ANNUAL REVIEWS

Annual Review of Fluid Mechanics

Continuum and Molecular Dynamics Studies of the Hydrodynamics of Colloids Straddling a Fluid Interface

Charles Maldarelli,[1] Nicole T. Donovan,[1]
Subramaniam Chembai Ganesh,[1] Subhabrata Das,[2]
and Joel Koplik[3]

[1] Department of Chemical Engineering and Levich Institute, The City College of The City University of New York, New York, NY, USA; email: cmaldarelli@ccny.cuny.edu

[2] Langmuir Center for Colloids and Interfaces, Columbia University, New York, NY, USA

[3] Department of Physics and Levich Institute, The City College of The City University of New York, New York, NY, USA

Annu. Rev. Fluid Mech. 2022. 54:495–523

The *Annual Review of Fluid Mechanics* is online at fluid.annualreviews.org

https://doi.org/10.1146/annurev-fluid-032621-043917

Keywords

colloidal hydrodynamics, molecular dynamics, Stokes flow, interfacial flow

Abstract

Colloid-sized particles (10 nm–10 μm in characteristic size) adsorb onto fluid interfaces, where they minimize their interfacial energy by straddling the surface, immersing themselves partly in each phase bounding the interface. The energy minimum achieved by relocation to the surface can be orders of magnitude greater than the thermal energy, effectively trapping the particles into monolayers, allowing them freedom only to translate and rotate along the surface. Particles adsorbed at interfaces are models for the understanding of the dynamics and assembly of particles in two dimensions and have broad technological applications, importantly in foam and emulsion science and in the bottom-up fabrication of new materials based on their monolayer assemblies. In this review, the hydrodynamics of the colloid motion along the surface is examined from both continuum and molecular dynamics frameworks. The interfacial energies of adsorbed particles is discussed first, followed by the hydrodynamics, starting with isolated particles followed by pairwise and multiple particle interactions. The effect of particle shape is emphasized, and the role played by the immersion depth and the surface rheology is discussed; experiments illustrating the applicability of the hydrodynamic studies are also examined.

1. INTRODUCTION

In this review we examine the literature on the hydrodynamics of colloids—here, particles of the order of 10 nm to 10 μm in characteristic size—that straddle a fluid interface, such as an air/water surface or an oil/water interface. As explained below, wetting forces can energetically trap straddling colloids partially immersed in the fluid phases bounding an interface, allowing for the formation of stable monolayers in which the particles resist moving normal to the surface, but translate and rotate along the surface. These motions are the focus of this review. As the range of colloid sizes spans from the nano- to the microscale, we focus on studies based on molecular dynamics (MD) and continuum frameworks. We begin with a short perspective on why this hydrodynamics is of interest.

From a scientific point of view, colloids that move and rotate along a fluid surface are paradigms for the dynamics of self-organization and assembly of particles on a 2D landscape as driven by in-plane forces. Forces that act on colloids at a fluid interface include thermal fluctuation (Brownian) forces and external forces such as electrostatic or magnetic forces acting along the surface on charged or magnetic particles. Interparticle forces become important when particles come close together; for reviews readers are referred to Kralchevsky & Nagayama (2000, 2001), Kralchevsky & Denkov (2001), Bresme & Oettel (2007), and Bleibel et al. (2013). These interparticle forces include capillary attraction due to the deformation of the interface as a result of the particle weight (Nicolson 1949, Chan et al. 1981, Blanc et al. 2013, Galatola & Fournier 2014) or undulations in the contact line attaching the interface to particles that are either floating (Stamou et al. 2000, Kralchevsky et al. 2001, Fournier & Galatola 2002, Danov & Kralchevsky 2010a) or resting on a solid support [immersion forces (Kralchevsky & Nagayama 1994, 2000, 2001; Kralchevsky & Denkov 2001)]. In addition, electrostatic repulsions develop between charged colloids (Foret & Wurger 2004; Oettel et al. 2005; Wurger & Foret 2005; Danov & Kralchevsky 2006, 2010b; Boneva et al. 2007, 2009; Dominguez et al. 2007; Oettel & Dietrich 2008), or magnetic repulsions develop if the particles are magnetic and magnetized by a external magnetic field (Vandewalle et al. 2012, 2013; Lumay et al. 2013; Darras et al. 2018).

Aside from their scientific interest, colloids at fluid interfaces have been the focus of significant technological attention because of their ability to form stable monolayers due to the fact that they are energetically entrapped at the surface. Early technological interest in them, dating back to over a century ago, was concerned with their use to stabilize foams and emulsions (see Binks 2002, Binks & Horozov 2006). Particles added to the continuous liquid phase of a foam, or the continuous or dispersed phases of an emulsion (Pickering emulsions), adsorb at the bubble or droplet interfaces, forming a monolayer that stabilizes the dispersed phase from coalescence and coarsening. Current and emerging applications, however, center around the structures formed as they assemble under the action of external and interparticle forces. Many experimental studies for spherical colloids at an air/water interface have demonstrated this assembly: At low particle surface concentrations, the colloids assemble into clusters, rafts, and foam-like meso-structures. At higher concentrations, they assemble into hexagonal crystalline lattices with particle separations of a few molecular diameters (see Pieranski 1980; Onoda 1985; Hórvölgyi et al. 1991, 1994; Ruiz-Garcia et al. 1997, 1998; Ghezzi et al. 2001; Chen et al. 2005, 2006). Their reorganization and buckling into multilayers due to surface compression (as on the surface of a Langmuir trough) have also been detailed. In all of these experiments, the liquid layers are deep (typically much larger than the particle diameter). Monolayers of spherical colloids have also formed at the interface between air and a thin liquid film of water or another solvent in which the film thickness is of the order of the particle diameter. These films are formed by either Langmuir–Blodgett dip-coating or by the forced spreading of films along a substrate (convective assembly). Evaporation of the liquid in the film reduces the interparticle distance and draws the particles together. Denkov et al. (1992, 1993) showed how well-packed crystalline monolayers can be formed from convective assembly. These assembled monolayers, in particular, have been utilized in applications such as coatings (superhydrophobic or antireflection), templates for micro- and nanostructured materials [e.g., nanosphere lithography (Burmeister et al. 1997)], and photonic crystals for optoelectronic devices (for reviews see Prevo et al. 2007).

While the forces that act on colloids trapped on an interface (Bresme & Oettel 2007, Danov & Kralchevsky 2010a), and the physico-chemistry of the particles, have been well studied (e.g., see the reviews Maestro et al. 2018, Ballard et al. 2019, Guzmán et al. 2021) and their rheological behavior has been characterized (Mendoza et al. 2014, Deshmukh et al. 2015), a fundamental understanding of the hydrodynamics of the straddling particles is only beginning to emerge. The purpose of this review is to summarize this emergent understanding. We begin (Section 2) by examining the equilibrium energetics of particles straddling a fluid interface, from both a continuum and an MD perspective. In Section 3, the hydrodynamics is discussed, focusing first on isolated particles and then on pairwise and multiparticle interactions. Most of the literature are continuum studies, but we also review recent work on MD simulations of the particle surface hydrodynamics. Finally, we examine experimental studies on the hydrodynamics (Section 4) and detail how theory can explain observations. We conclude with a perspective on future directions of this area of research (Section 5).

2. THE EQUILIBRIUM CONFIGURATION OF COLLOIDS AT A FLUID INTERFACE

When a colloid particle adsorbs at a fluid interface, the equilibrium position that it achieves is a function of its shape, the wettability of the surface of the particle relative to the phases that bound the interface, and the tension of the fluid interface. In **Figure 1** we illustrate this surface equilibration, from both continuum and MD frameworks, using a sphere of radius a that is uniform in its surface properties and atop a flat fluid interface (surface tension γ_{f}) with bounding immiscible phases (1, lower; 2, upper) and immersion depth d measured from the particle center to the interface (d is positive when the center is in the lower phase).

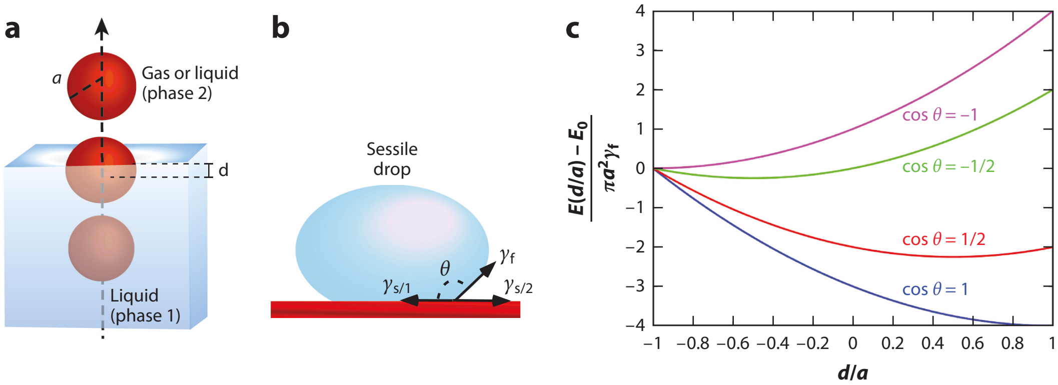

Figure 1

(*a*) Schematic representation of a sphere of radius a breeching a fluid interface separating two phases (1, lower; 2, upper) at an immersion depth d. (*b*) Young–Dupré balance of forces at the contact line, $\gamma_{s/2} - \gamma_{s/1} = \gamma_{\mathrm{f}} \cos\theta$. (*c*) Interfacial energy $E(d)$ as a function of d and contact angle θ.

Review in Advance first posted on
November 18, 2021. (Changes may
still occur before final publication.)

In the continuum framework (**Figure 1*a***), the interfacial energy E of the sphere as a function of immersion depth d, relative to its energy when it is completely in the upper phase (E_0; $d/a = -1$), can simply be calculated in terms of the tension of the fluid interface γ_{f} and the interfacial energies of the surface in contact with the upper ($\gamma_{\mathrm{s}/2}$) and lower ($\gamma_{\mathrm{s}/1}$) phases,

$$E(d/a) - E_0 = -\gamma_{\mathrm{f}}\pi a^2\left[1-\left(\frac{d}{a}\right)^2\right] + 2\pi a^2\left(1-\frac{d}{a}\right)(\gamma_{\mathrm{s}/1}-\gamma_{\mathrm{s}/2}),$$

where E_0 is the interfacial energy of the sphere in the upper (2) phase ($4\pi a^2\gamma_{\mathrm{s}/2}$). The terms on the right-hand side of this equation illustrate the competing effects as the colloid locates through the surface: The first term represents the reduction in energy due to the removal of the fluid surface by the breeching sphere, and the second term represents the difference in surface energies as the interfacial area of the upper phase in contact with the sphere is replaced by the lower phase. The interfacial energy difference, $\gamma_{s/1} - \gamma_{s/2}$, can be written in terms of the contact angle θ on the solid surface, as is clear from the Young–Dupré balance of forces on the sessile drop configuration (**Figure 1*b***), $\gamma_{s/2} - \gamma_{s/1} = \gamma_{\mathrm{f}}\cos\theta$. As such, θ represents the relative wettability of the two phases for the surface s. For $\theta = 0°$ the lower fluid completely wets the surface, and for $\theta = \pi$ the upper fluid completely wets the surface; values between these characterize partial wetting. In **Figure 1*c***, $E(d/a) - E_0$ is plotted for different contact angles, and it is clear that particles with surfaces of intermediate wettability have a minimum in the interfacial free energy at a straddling position $-1 < d/a < 1$. This position is found from differentiation to be located at $d_{\mathrm{eq}}/a = \cos\theta$ and the energy minimum is equal to $E(d_{\mathrm{eq}}/a) - E_0 = -\gamma_{\mathrm{f}}\pi a^2(1+\cos\theta)^2$. Thus, for intermediate wettability, the sphere straddles the fluid interface such that it achieves its equilibrium angle on the solid surface of the particle. This derivation assumes that there are no other forces on the particle or fluid; it can easily be extended to include gravitational, electrostatic, and magnetic forces, in which the interface deforms around the particle.

Three important points relative to the above simple derivation are important to note. First, for particles that are partially wetting, $-1 < \cos\theta < 1$, the magnitude of the adsorption energy $\gamma_{\mathrm{f}}\pi a^2(1+\cos\theta)^2$ is typically much larger than the thermal energy $k_{\mathrm{B}}T$, and as such, the particles—either deposited directly on the interface or adsorbed from the fluid phases—remain trapped at the interface, moving freely along only the plane of the surface (Binks 2002). Second, the discussion of the contact line is oversimplified: Most colloid surfaces are rough rather than smooth or contain chemical heterogeneities, and these heterogeneities lead to a deformation of the fluid interface in the immediate vicinity of the particle as the contact line adjusts to the surface protrusions or chemical imperfections to satisfy equilibrium. The surface heterogeneities create local minima in the free energy, and particles placed on the interface can show a slow equilibration as they become trapped in these minima (Kaz et al. 2012, Colosqui et al. 2013, Rahmani et al. 2016). Third, the direct measurement of contact angles on the surfaces of particles is difficult (for reviews, see Maestro et al. 2014): For large particles (greater than $\sim 10^2$ μm), the contact angle can be obtained directly by visualization. Other techniques have been developed for colloids tens of micrometers and smaller. These include optical microscopy techniques based on interference patterns created between the interface and a reference surface [e.g., vertical scanning interferometry (Boniello et al. 2015)] or patterns generated between the meniscus and a surface underlying the interface (Hadjinski et al. 1996, Ally & Amirfazli 2010), digital holography (Kaz et al. 2012, Rahmani et al. 2016), and measurements of the curvature and direction of the wavefront produced by the particle (Snoeyink et al. 2015). A second set of techniques is based either on trapping the particle at the interface by gelling the underlying subphase and imaging the immobilized particles by atomic force microscopy (AFM) or scanning electron microscopy to obtain the immersion depth (Paunov 2003), or on immobilizing the particle by jet-freezing followed by fracturing and shadow casting to obtain this depth (Isa et al. 2011).

For nanoparticles straddling a fluid interface, MD can be used to formulate and minimize interfacial energies to obtain equilibrium immersion depths. MD studies can be used to validate predictions of the continuum theory when extended to the nanoscale and to provide molecular insights not revealed by the continuum framework. We use the study of Koplik & Maldarelli (2017) to illustrate this point. Koplik & Maldarelli's (2017) MD effort studied a gas/liquid interface with the liquid comprising a tetramer of atoms (species 1) tethered together by a FENE (finitely extensible nonlinear elastic) potential and interacting with each other by a Lennard–Jones (LJ) potential, $V_{\mathrm{LJ}}(r) = 4\epsilon[(r/\sigma)^{-12} - c_{ij}\,(r/\sigma)^{-6}]$, where σ is the atom diameter (the same for all atoms), ϵ is the common energy scale, r is the separation distance between atoms, and the coefficients c_{ij} adjust the strength of the attractive interaction between atoms of atomic species i and j ($c_{11} = 1$). The solid particle (species 2) was a rigid spherical section of a cubic lattice of LJ atoms constructed by enclosing all atoms of the lattice within a radius 8σ of a central atom. The nanoparticle atoms interacted with the tetramer via the LJ potential with the same energy ϵ but with an attractive interaction strength c_{12}. This interaction strength was changed to provide different wettabilities and immersion depths. The bottom face-centered cubic lattice consisted of atoms (species 4) attached by linear tether springs to the lattice sites and with interactions with the other atoms given by coefficient of attraction $c_{i4} = 1$. All atoms had a common mass m. The simulation box (**Figure 2*a***) was a cube of side 60.3σ, and a Nose–Hover thermostat fixed the temperature to $0.8\epsilon/k_{\mathrm{B}}$, at which the tetramer liquid and vapor were in equilibrium. The vapor/liquid surface tension (calculated through numerical integration of the normal and transverse stress across the interface) was $\gamma_{\mathrm{f}} = 0.668\epsilon/\sigma^2$, the bulk liquid density was $0.857\sigma^{-3}$, and the viscosity was $\eta = 5.18m/(\sigma\tau)$ [obtained by simulating Couette flow between plates as $\tau = \sigma(m/\epsilon)^{1/2}$] for $c_{11} = 1$.

From the MD simulations, the immersion could be computed in several ways. In the direct method, the nanoparticle was initially placed in the liquid layer and allowed to migrate upward to its equilibrium position on the interface and diffuse along the surface. The height fluctuations during the surface diffusion had a standard deviation in the height distribution of at most 0.6σ, and furthermore, the interface remained approximately flat up to the colloid surface. An immersion depth can be calculated based on the average horizontal position of the center of the particle relative to isosurfaces of the fluid density far from the interface (see **Figure 2*b*** for $c_{12} = 0.9$). Note that since the particle radius a is comparable to the size of the interfacial transition zone, the different isosurfaces intersect the particle at different positions and contact angles; hence, a convention is required. We define the immersion depth as the vertical distance from the half-bulk-density isosurface to the particle center, giving an apparent contact angle of $d/a = \cos\,\theta_{\mathrm{A}}$, which is given in **Figure 2*e*** as a function of c_{12}. Immersion into the liquid increased with c_{12}, as was also shown by Cheng & Grest (2012). In contrast, in conventional MD simulations of sessile drops on a planar substrate, there is no ambiguity because all isocontours intersect the surface at nearly identical angles. In **Figure 2*c*** we illustrate this fact by showing the isocontours of a tetramer liquid drop on a substrate identical to the colloid with the same lattice configuration for $c_{12} = 0.9$. Using sessile drop simulations we can define a contact angle θ_{SD}, which is given in **Figure 2*e***.

In the MD framework, the immersion depth can also be calculated by obtaining the free energy as a function of the vertical position of the center of the colloid z_{p} by thermodynamic integration (Razavi et al. 2013): $\Delta\mathcal{F} = \int \mathbf{F}(\mathbf{r}) \cdot d\mathbf{r}$, where $\mathbf{F}$ is the force on the particle at $\mathbf{r}$. In calculating the integral, one first places the particle in the nearly empty region above the interface, then it is slowly displaced downward into the liquid, reequilibrating the system; finally, the force is averaged while it is held at that position. The results are given in **Figure 2*d*** for various wettabilities, with distance measured in units of σ from the bottom of the computational domain and the interface at

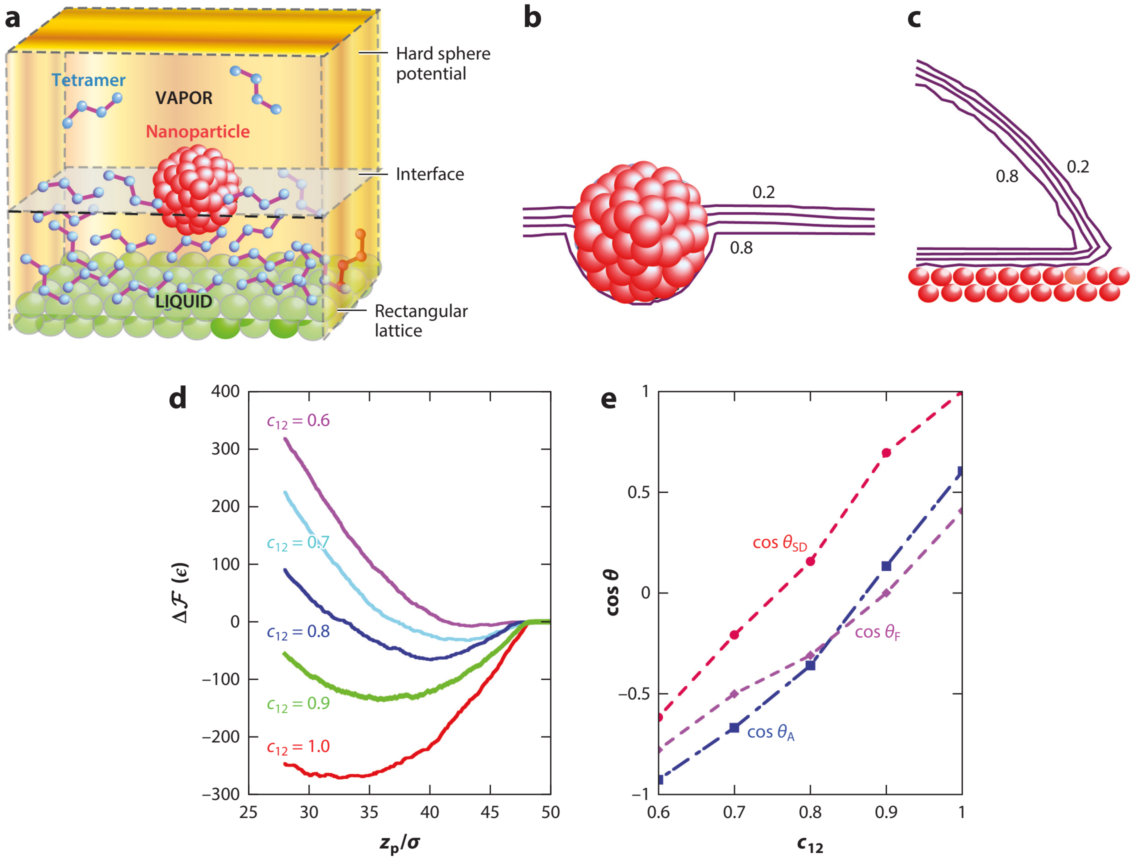

Figure 2

Molecular dynamics (MD) simulations for a nanoparticle interacting with tetramers. (*a*) Computational domain showing liquid tetramers, a layered lattice floor, and a nanoparticle constructed from a face-centered cubic lattice of atoms of diameter σ. (*b*) Isocontours of density at the interface in units of σ^{-3} for $c_{12} = 0.9$, the coefficient of the strength of the attractive interaction between the tetramers (atomic species 1) and the nanoparticle (atomic species 2). (*c*) Sessile drop simulation of tetramer liquids atop a solid with the same atoms and lattice structure as the nanoparticle, showing the isocontours of density in the same units and value of c_{12} as panel *b*. (*d*) Energy $\Delta\mathcal{F}(\epsilon)$ relative to immersion in the vapor phase as a function of position through the interface, z_p/σ. (*e*) Contact angles θ obtained from energy minimization (F), the position of the nanoparticle at the interface (A), and the sessile drop configuration (SD) for different values of c_{12}. Figure adapted with permission from Koplik & Maldarelli (2017).

$z_p \approx 40\sigma$. The curves become flat for lower values of z fully inside the bulk liquid. A contact angle based on the free energy minimum, $\Delta\mathcal{F}/(\pi a^2\gamma) = -(1 + \cos\theta_F)^2$, is also plotted in **Figure 2*e***, and fairly good agreement is obtained for each of the methods.

Three important points can be concluded from the MD simulations: First, even for the lowest wettabilities ($c_{12} = 0.6$) the particle remains trapped at the surface, translating and rotating only along the surface. Second, the simulation of the change in energy as the particle is positioned through the interface agrees remarkably with the continuum picture. Third, nanoparticles can span the interfacial zone defined by the density; when we examine their translation and rotation, the fact that they are not partially immersed in a bulk liquid affects their hydrodynamics.

The above studies examined colloids that were chemically homogeneous; recent attention has focused on Janus colloids, in which the particle surface contains two faces, one with a small contact

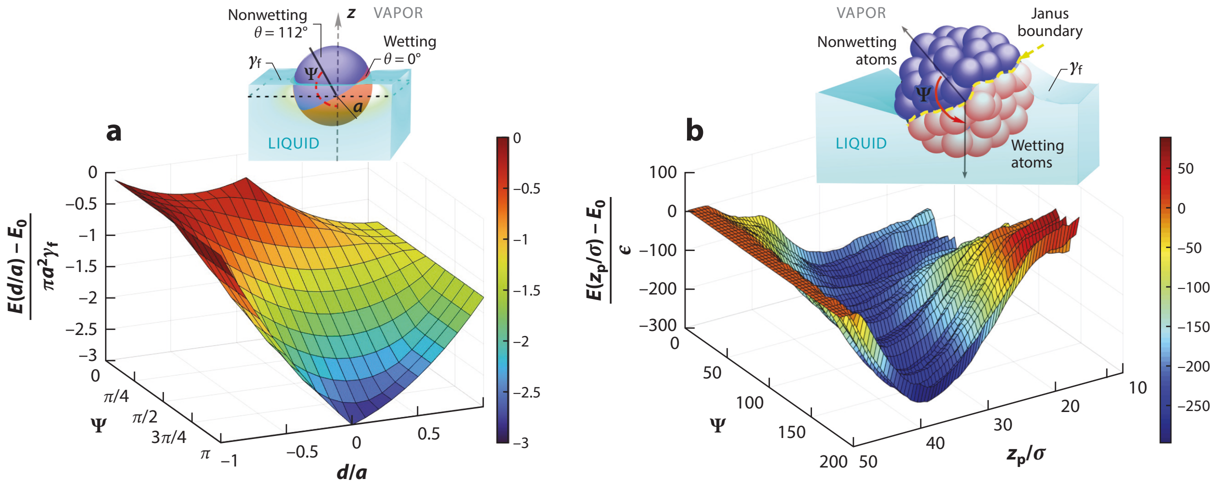

Figure 3

Continuum (*a*) and molecular dynamics (MD) (*b*) simulations of the interfacial energy of a Janus particle of radius *a* with hemispheres that wet or do not wet the liquid. The energies are a function of the orientation angle Ψ and the immersion depth (d/a for the continuum calculation and position z_p/σ for the MD calculation). Figure adapted with permission from Koplik & Maldarelli (2019).

angle with the liquid phase (a wetting face), and one with a large contact angle with the liquid phase (a nonwetting face). In **Figure 3*a***, we illustrate an example in which one hemisphere is nonwetting to the liquid ($\theta = 112°$), and one is wetting ($\theta = 0°$). Note that for the Janus particle, the interfacial energy is a function of the orientation angle Ψ (the angle between the symmetry axis of the Janus colloid and the interface) and the distance from the particle center to the interface (d/a). For the continuum simulation (**Figure 3*a***), the energy calculation begins at $\Psi = 0°$ and $d/a = -1$, which corresponds to the nonwetting side down and an initial position of the particle completely in the vapor phase. Initially, the energy decreases because of the change in interfacial area when the particle just breaches the interface between fluids 1 and 2. At $\Psi = 0°$, the interaction of the nonwetting face of the particle and the liquid as d/a increases to 0 soon overwhelms the effect of the reduced interfacial area on the total change in energy. This increasingly unfavorable interaction therefore represents a local maximum in the interfacial free energy. As d/a tends to 1, the wetting side of the Janus sphere favorably contacts the liquid, hence the decrease in energy. As the orientation angles increases to π, the wetting area of the particle becomes more exposed to the liquid at $d/a = 0$ and the energy decreases as a result. The lowest free energy occurs at $\Psi = \pi$, where the wetting face is in complete contact with the liquid. More specifically, at an immersion depth of 0 (therefore $d/a = 0$), the particle rests with all the wetting area in the liquid phase and all the nonwetting area in the vapor phase. This location also corresponds to the largest reduction in the interfacial area by the particle, since the cross-sectional area of the particle is largest through the particle center. As seen in **Figure 3*a***, the result is a sharp minimum in free energy. It is worth noting that the preferred Janus configuration of particles at $\Psi = \pi$ leads to a lower energy minimum than the case where the particle surface is uniform with a contact angle of $\theta = 112°$.

For the MD calculation (Koplik & Maldarelli 2019; **Figure 3*b***) the Janus colloid is formed from two sets of atoms forming cubic latices filling the hemispheres of the colloid: one set (labeled 2) with a wetting interaction with a tetramer solvent ($c_{12} = 1.2$, contact angle $\theta_\mathrm{F} = 0°$), as determined from the minimum interfacial energy of a particle made of only these atoms, and another set (labeled 3) with a nonwetting interaction ($c_{12} = 0.8$, contact angle $\theta_F = 112°$). The results of the thermodynamic integration for the interfacial energy (divided by the MD energy scale ϵ) are shown in **Figure 3*b***, and the landscape has the same features as the continuum plot. However, the minimum for $\Psi = \pi$ and $z_p \approx 40$ (the location of the free surface in the absence of the particle) is approximately 240ϵ or

$$\frac{E(d/a) - E_0}{\pi \gamma_f a^2} = -1.79,$$

which is greater than the continuum value of -3.0. The reason that the depth (and position) of the minimum differs arises from the variation in liquid density near the minimum in the MD simulations. There, the liquid has lower density near the contact line and exerts less attractive force on the colloid. The free energy minimum occurs when the lower wetting half is immersed, which requires a deeper depth relative to the distant interface, and at this point the liquid/vapor interface is distorted, which incurs an additional free energy cost.

3. THEORETICAL STUDIES OF THE HYDRODYNAMICS OF PARTICLES AT AN INTERFACE

We begin by examining the continuum theories for the translation and rotation of particles straddling a fluid interface. MD simulations are discussed in Section 3.6. The flow generated by the surface movement of the colloids is typically inertialess; hence, the starting point of continuum models are, assuming the bounding fluids are Newtonian and incompressible, the Stokes and continuity equations. Attention has focused principally on motion along flat interfaces, with the immersion depth assumed constant (as determined by the balance in interfacial energies), and with the interface remaining flat up to the contact line (viscous forces are small relative to surface tension forces—capillary numbers are small). With these assumptions, the flow can be understood (due to the linearity of the Stokes equations) as a sum of separate flow realizations. Here we discuss this decomposition in the context of a sphere, although the discussion can be easily extended to colloids of arbitrary shape, as we discuss below. **Figure 4** illustrates the three general motions for a sphere: (*a*) translation along the interface in the z-direction with velocity $U\mathbf{e}_z$, (*b*) rotation around an axis parallel to the interface (and through the particle center) with angular velocity $\Omega_\parallel \mathbf{e}_y$, and (*c*) rotation around an axis (x) perpendicular to the interface (and through the particle center) with angular velocity $\Omega_\perp \mathbf{e}_x$. As in the previous section, a is the sphere radius, the lower phase is denoted by $i = 1$ and the upper phase by $i = 2$, the bounding fluid viscosities are denoted by μ_i, and $d/a = \cos\theta$ denotes the immersion depth measured from the sphere center to the interface (which is positive when the center is in the lower phase) as determined from the contact angle θ. In this section, we focus on the first two canonical motions (*a* and *b*); the third is straightforward, does not involve any drag due to the rotation, and has been treated by Zabarankin (2007).

For each of these motions, the resulting hydrodynamic flow is described by solving the Stokes and, assuming the fluids are incompressible, mass conservation equations:

$$-\nabla p_i + \mu_i \nabla^2 \mathbf{v}_i = 0, \qquad 1.$$

$$\nabla \cdot \mathbf{v}_i = 0, \qquad 2.$$

where ∇ is the Laplacian operator and μ_i, p_i, and $\mathbf{v}_i$ are respectively the viscosity, pressure, and velocity of phase i. Along the fluid interface with unit normal and tangential vectors $\mathbf{n}_{(s)}$ and $\mathbf{t}_{(s)}$, respectively, for all three realizations in **Figure 4**, the normal velocity is zero for each phase, and

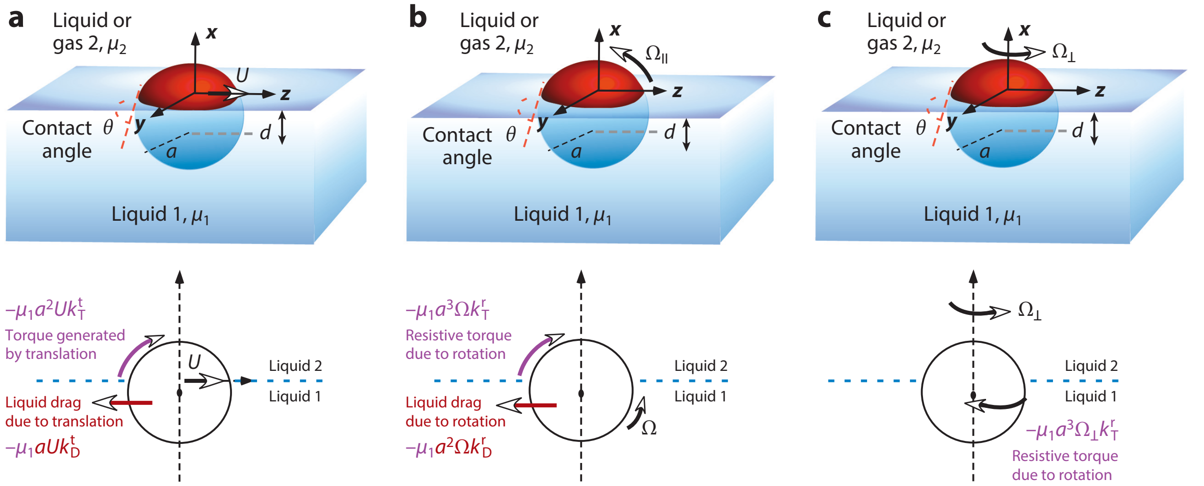

Figure 4

A sphere of radius *a* immersed in a liquid at an immersion depth *d* set by its contact angle θ (*a*) translating at velocity $U\mathbf{e}_z$, (*b*) rotating around an axis through the sphere center parallel to the interface with angular velocity $\Omega_\parallel \mathbf{e}_y$, and (*c*) rotating with angular velocity $\Omega_\perp \mathbf{e}_x$ around an axis through the sphere center perpendicular to the interface (*top*, schematic representations; *bottom*, the associated free body diagrams). The viscosities of the upper (liquid 2) and lower (liquid 1) phases are denoted by μ_2 and μ_1, respectively. Figure adapted with permission from Das et al. (2018).

the tangential velocity and shear stress are continuous:

$$\mathbf{n}_{(\mathrm{s})} \cdot \llbracket \mathbf{v}_{(\mathrm{s})\mathrm{i}} \rrbracket = 0, \qquad 3.$$

$$\mathbf{t}_{(\mathrm{s})} \cdot \llbracket \mathbf{v}_{(\mathrm{s})i} \rrbracket = 0, \qquad 4.$$

$$\mathbf{n}_{(\mathrm{s})} \cdot \llbracket \boldsymbol{\tau}_{(\mathrm{s})i} \rrbracket \cdot \mathbf{t}_{(\mathrm{s})} = 0, \qquad 5.$$

where we have $\boldsymbol{\tau}_i = \mu_i(\nabla\mathbf{v}_i + \nabla\mathbf{v}_i^\dagger)$, the subscript s denotes that the quantity is evaluated at the surface, and the double brackets indicate a difference across the interface (phase 2 minus phase 1).

At the particle surface, for the translational motion, the normal velocity of the fluid at the particle surface is equal to the normal velocity of the particle, and for the rotational motion, the normal velocity is equal to zero:

$$\mathbf{n}_{(\mathrm{p})} \cdot \left[\mathbf{v}_{(\mathrm{p})i} - U\mathbf{e}_z\right] = 0, \qquad 6.$$

$$\mathbf{n}_{(\mathrm{p})} \cdot \left[\Omega_\parallel \mathbf{e}_y \times \mathbf{r}_{(\mathrm{p})} - \mathbf{v}_{(\mathrm{p})i}\right] = 0, \qquad 7.$$

where $\mathbf{v}_{(\mathrm{p})i}$ denotes the fluid velocity evaluated at the section of the surface that intersects phase *i*, and $\mathbf{n}_{(\mathrm{p})}$ and $\mathbf{r}_{(\mathrm{p})}$ are respectively the unit normal to the particle surface and the vector from the particle center to the surface. The usual assumption for the fluid velocity tangent to the surface of the particle is that there is no slip—the tangential velocity of the fluid equals that of the particle. For the translational motion of the particle (**Figure 4*a***), the use of this boundary condition does not give rise to stress singularities at the contact line because there is no movement of the contact line relative to the surface. Thus, we can apply the no-slip condition, $\mathbf{t}_{(\mathrm{p})} \cdot \left[\mathbf{v}_{(\mathrm{p})i} - U\mathbf{e}_z\right] = 0$, where $\mathbf{t}_{(\mathrm{p})}$ is a unit vector tangent to the surface and $\mathbf{v}_{(\mathrm{p})i}$ is the velocity of liquid *i* at the particle surface. However, for the rotational motion (**Figure 4*b***), along one face of the sphere the meniscus recedes and along another face it advances. The resultant velocity field at the contact line results in a nonintegrable stress singularity at the surface, which results in the torque required to rotate the particle tending to infinity. To alleviate this singularity, the liquid can be assumed to slip over the surface. The phenomenon of slip has been of long-standing interest, most recently with regard to drag reduction (for reviews, see Lauga et al. 2007, Lee et al. 2014). In a continuum formulation, slip follows the Navier formulation:

$$\begin{aligned}\mathbf{t}_{(\mathrm{p})} \cdot \left[\mathbf{v}_{(\mathrm{p})i} - U\mathbf{e}_z\right] &= \lambda \left[\mathbf{n}_{(\mathrm{p})} \cdot \boldsymbol{\tau}_{(\mathrm{p})i} \cdot \mathbf{t}_{(\mathrm{p})}\right],\\ \mathbf{t}_{(\mathrm{p})} \cdot \left[\Omega_{\|}\mathbf{e}_y \times \mathbf{r}_{(\mathrm{p})} - \mathbf{v}_{(\mathrm{p})i}\right] &= \lambda \left[\mathbf{n}_{(\mathrm{p})} \cdot \boldsymbol{\tau}_{(\mathrm{p})i} \cdot \mathbf{t}_{(\mathrm{p})}\right].\end{aligned} \qquad 8.$$

Here, the difference between the surface velocity and the fluid at the surface in a tangential direction is equal to a slip coefficient λ (with units of length) multiplied by the shear stress $\boldsymbol{\tau}_{(\mathrm{p})i}$ exerted on the surface in that tangential direction. (In this formulation, we assume implicitly that the slip length is the same for both phases bounding the interface.) MD simulations on atomically smooth surfaces have demonstrated slip on the molecular scale and have calculated λ as a function of the strength of the liquid/solid interaction (e.g., Voronov et al. 2007, Sendner et al. 2009). For strong liquid/solid interactions that characterize complete or strong wetting of the liquid on the solid surface, slip lengths are of the order of only a few molecular diameters [$\mathcal{O}(1\ \mathrm{nm})$], while relatively weaker interactions of partially wetting fluids have slip lengths extending tens of diameters [$\mathcal{O}(10\ \mathrm{nm})$]. Current tools for measuring λ include particle image velocimetry, image velocimetry enhanced with evanescent near-field illumination at the surface, AFM, and surface force apparatus measurements (Neto et al. 2005). Several experiments are consistent with the MD calculations. For smooth surfaces of a wetting liquid (e.g., water flowing along a hydrophilic surface), either zero slip or coefficients less than a few nanometers are recorded, while for water over a partially wetting hydrophobic surface (e.g., self-assembled octadecyl silane monolayers), slip lengths of tens of nanometers are obtained (e.g., Vinogradova & Yakubov 2003, Cottin-Bizonne et al. 2005, Huang et al. 2006, Bouzigues et al. 2008). For nonpolar liquids wetting smooth hydrophobic surfaces (the weakest liquid/surface interactions), slip lengths are of the order of a few tens of nanometers (McBride & Law 2009, Bowles et al. 2011, Zhu et al. 2012). Colloids adsorbing and straddling an interface show intermediate wettability to each phase; hence, slip lengths of the order of tens of nanometers are expected. Thus, slip lengths relative to the colloid radius would be of order 0.01 for a particle of radius 1 μm. However, it is important to note that the surface of colloids can be rough, and as such, the contact line can be pinned by the surface roughness. In this case the particle is not free to rotate and the torque on the particle generated by the translation is balanced by the surface tension forces exerted by the meniscus asymmetrically over the particle surface. This point has been discussed by Dörr & Hardt (2015), and MD simulations detailed below in Section 3.6 provide an example of this pinning for nanoparticles with rough surfaces.

From the solution for the flow field, the drag and torque exerted on the particle in the two flow realizations can be computed straightforwardly as

$$F_{(\mathrm{p})z} = \sum_{1}^{2} \iint_{\Omega_i} \left(-p_i\mathbf{n}_{(\mathrm{p})} + \mathbf{n}_{(\mathrm{p})} \cdot \boldsymbol{\tau}_{(\mathrm{p})i}\right) \cdot \mathbf{e}_z \mathrm{d}\Sigma_i, \qquad 9.$$

$$T_{(\mathrm{p})y} = \sum_{1}^{2} \iint_{\Omega_i} \left[\mathbf{r}_{(\mathrm{p})} \times \left(-p_i\mathbf{n}_{(\mathrm{p})} + \mathbf{n}_{(\mathrm{p})} \cdot \boldsymbol{\tau}_{(\mathrm{p})i}\right)\right] \cdot \mathbf{e}_y \mathrm{d}\Sigma_i, \qquad 10.$$

respectively, where Σ_i is the surface area of the particle adjoining the bottom ($i = 1$) or top ($i = 2$) phases. For the translational motion in the $+z$-direction (**Figure 4*a***), the fluids bounding the interface exert a drag in the opposite ($-z$) direction, defining a drag coefficient $k^{\mathrm{t}}_{\mathrm{D}}$ by the relationship $F_{(\mathrm{p})z} = -\mu_1 a k^{\mathrm{t}}_{\mathrm{D}} U$. This translational motion also generates a torque around an axis parallel to the y-direction and through the particle center that acts to rotate the particle. This torque arises because the shear stresses exerted by the bounding liquids on the sphere are asymmetric due to the difference in the liquids' viscosities, and a torque drag coefficient $k^{\mathrm{t}}_{\mathrm{T}}$ is defined by $T_{(\mathrm{p})y} = -\mu_1 a^2 k^{\mathrm{t}}_{\mathrm{T}} U$. The rotational motion (**Figure 4*b***) generates a resistive torque around the axis passing through the sphere center and in the y-direction, as defined by $T_{(\mathrm{p})y} = -\mu_1 a^3 k^{\mathrm{r}}_{\mathrm{T}} \Omega$, where $k^{\mathrm{r}}_{\mathrm{T}}$ is the resistive torque coefficient due to rotation. Finally, due to the rotation, a drag in the z-direction is exerted by the bounding fluids due to the shear stress generated by the motion and is given by $F_{(\mathrm{p})z} = -\mu_1 a^2 k^{\mathrm{r}}_{\mathrm{D}} \Omega$, where $k^{\mathrm{r}}_{\mathrm{D}}$ is the drag coefficient due to the rotational motion. These drag coefficients are assembled in a matrix form that defines the net forces and torques on the particle:

$$\begin{bmatrix} F^{\mathrm{T}}_{(\mathrm{p})z} \\ T^{\mathrm{T}}_{(\mathrm{p})y}/a \end{bmatrix} = -a\mu_1 \begin{bmatrix} k^{\mathrm{t}}_{\mathrm{D}} & k^{\mathrm{r}}_{\mathrm{D}} \\ k^{\mathrm{t}}_{\mathrm{T}} & k^{\mathrm{r}}_{\mathrm{T}} \end{bmatrix} \begin{bmatrix} U \\ a\Omega \end{bmatrix}, \qquad 11.$$

where the T superscript indicates the total drag on the particle. All four coefficients are a function of the nondimensional groups, the scaled immersion depth (d/a), the slip coefficient (λ/a), and the ratio of the viscosity of the upper to the lower phase ($\beta = \mu_2/\mu_1$).

3.1. Single Particle Half-Immersed at a Clean Fluid Interface

Consider first spherical colloids. If their surfaces are neutrally wetting ($\theta = \pi/2$), then the colloid straddles the surface symmetrically with the interface as its mirror plane ($d = 0$). In this case, one can take advantage of the symmetry to analytically describe the translation and rotation of the particles. In this section, we focus on clean fluid interfaces (see below for fluid interfaces with amphiphilic monolayers and bilayers). For the translational motion, if the fluid viscosities are equal ($\beta = 1$), then the flow is symmetric about the interface and the drag forces on the two halves of the sphere above and below the interface are equal and can be expressed as $\frac{1}{2}k^{\mathrm{t}}_{\mathrm{D}}(d = 0, \beta = 1, \lambda/a)\mu a U$. From the solution for the Stokes drag on a sphere in an infinite uniform medium (which is identical to this symmetric case), the drag coefficient on each half is $3\pi(1 + 2\lambda/a)/(1 + 3\lambda/a)$. The torques exerted on each half of the particle due to the translation (about the y-axis) are equal in magnitude and opposite in sign so that the net torque is equal to zero. From the solution for the translational motion of the particle in an infinite medium, the torque exerted on each half of the sphere around the y-direction is given by $\pm(3\pi/2)[1/(1 + 3\lambda/a)]\mu a^2 U$. Since the flow is symmetric about the (mirror) fluid plane, the shear stress at the interface in this flow field is zero. In this symmetric solution, for the flow fields in each fluid phase bounding the interface, in the case of no slip, the velocity field is independent of viscosity since the boundary conditions at the sphere surface (velocity equal to particle velocity) and the fluid interface (zero normal velocity and zero shear stress) are all independent of viscosity. The pressure distribution is then derived from the velocity distribution and is linear in the viscosity. For translating particles at half-immersion for the case in which the viscosities of the bounding fluids are different, this same symmetric hydrodynamic solution for the velocity field is valid for each region (since the boundary conditions are independent of viscosity). Thus, the drag and torque can be obtained by summing the contributions on each half for the corresponding viscosities. The drag is therefore given by $F_{(\mathrm{p})z} = \frac{1}{2}k^{\mathrm{t}}_{\mathrm{D}}(d = 0, \beta = 1, \lambda/a = 0)(\mu_1 + \mu_2)aU = 3\pi(\mu_1 + \mu_2)aU$, or $k^{\mathrm{t}}_{\mathrm{D}}(d = 0, \beta, \lambda/a = 0) = 3\pi(1 + \beta)$, and the generated torque is equal to $T_{(\mathrm{p})x} = 3\pi/2(\mu_1 - \mu_2)a^2 U$, or $k^{\mathrm{t}}_{\mathrm{T}}(d = 0, \beta, \lambda/a = 0) = 3\pi/2(1 - \beta)$. For the important case of a sphere symmetrically straddling a gas/liquid interface ($\mu_2 = 0$), the hydrodynamic force on the upper half of the sphere is zero, and from the above arguments and

Review in Advance first posted on
November 18, 2021. (Changes may
still occur before final publication.)

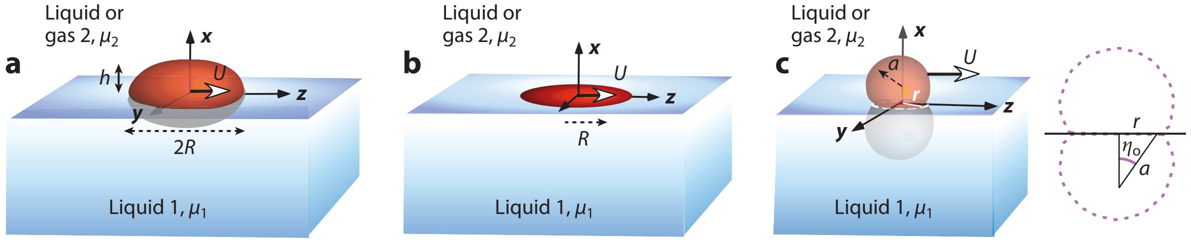

Figure 5

Symmetrically placed bodies of revolution partially immersed in a liquid of viscosity μ_1 below a liquid of viscosity μ_2. Schematic representation of (*a*) an oblate ellipsoid, (*b*) a disk of radius R, and (*c*) fused spheres of radius a and a contact radius r, all translating at velocity $U\mathbf{e}_z$.

by noting the gas/liquid interface is stress free, we can determine the drag coefficient to be

$$k^{\mathrm{t}}_{\mathrm{D}}(d=0,\ \beta=0,\ \lambda/a)=3\pi\,\frac{1+2\lambda/a}{1+3\lambda/a}$$

and the torque coefficient to be

$$k^{\mathrm{t}}_{\mathrm{T}}(d=0,\ \beta=0,\ \lambda/a)=\frac{3\pi}{2}\,\frac{1}{1+3\lambda/a}.$$

The symmetry arguments used above are not applicable to the case of imposed rotation about the y-axis since the shear stress at the fluid interface is not stress-free and the slip boundary condition involves the viscosity. However, the rotational problem can still be solved analytically by eigenfunction expansion in Gegenbauer polynomials, which has been undertaken for a tangential-stress-free interface using the Navier model for slip at the rotating surface of the sphere (O'Neill et al. 1985). The resistive torque due to the rotation was computed by series summation as a function of λ and diverges as the slip length decreases to zero owing to the contact line singularity with a correlated logarithmic divergence: $k^{\mathrm{r}}_{\mathrm{T}}=K_1\ln(a/\lambda)+K_2$ as λ tends to 0, with $K_1\approx 4.5$ and $K_2\approx 2.5$. The drag in the z-direction generated by the motion was found to equal

$$k^{\mathrm{r}}_{\mathrm{D}}(d=0,\beta=0,\lambda/a)=\frac{3\pi}{2}\,\frac{1}{1+3\lambda/a}=k^{\mathrm{t}}_{\mathrm{T}},$$

as required by reciprocity.

Aside from the sphere symmetrically straddling the fluid interface, other particle shapes have been studied that are symmetric about a plane dividing the particle and straddle the surface with the interfacial plane coincident with the mirror plane. These symmetric shapes are bodies of revolution and include the oblate ellipsoid (generated by rotation about the minor axis of an ellipse), the degenerate form (a circular disk), and fused spheres (**Figure 5**). As with the sphere, the symmetry of the configuration in these cases allows for analytical solutions but only for the translation along the surface. Again, these solutions require that (aside from the circular disk) the contact angle at the intersecting perimeter equals $\pi/2$ and, therefore, that the particle surface (assumed uniform in its wettability) is neutrally wetting with respect to the two phases bounding the interface.

For the oblate ellipsoid (**Figure 5*a***), defining h to be the protrusion above the interface, and R the radius of the contact line on the surface, and $\epsilon=h/R$, the drag on the spheroid for motion in the z-direction is given by (Stone & Ajdari 1998, Happel & Brenner 2012, Stone & Masoud 2015, Dörr et al. 2016)

$$F_{(\mathrm{p})z}=8\,[\mu_1+\mu_2]\,\pi RU\left[\frac{3-2\varepsilon^2}{(1-\varepsilon^2)^{3/2}}\arcsin\left(\sqrt{1-\varepsilon^2}\right)-\frac{\varepsilon}{1-\varepsilon^2}\right]^{-1}, \qquad 12.$$

$$F_{(\mathrm{p})z} = \frac{16}{3}(\mu_1 + \mu_2)RU\left[1 + \frac{8}{3\pi}\varepsilon + \mathcal{O}(\varepsilon^2)\right] \qquad (\varepsilon \ll 1), \tag{13.}$$

where the case $\varepsilon \ll 1$ describes an oblate shape only protruding a small distance into the bound fluid phases relative to the contact line radius. For the case of $\varepsilon \to 0$, the drag on a circular disk (**Figure 5*b***) is obtained as $F_{(\mathrm{p})z} = 16/3(\mu_1 + \mu_2)RU$, as originally derived by Ranger (1978).

For fused spheres that intersect as a cusp along the contact perimeter (**Figure 5*c***) at the fluid interface with angle η_0 and radius r equal to $a \sin \eta_0$, Zabarankin (2007) has obtained an analytical solution for the drag due to motion in the z-direction using a Mehler–Fock integral transform of the Stokes equations written in toroidal coordinates (the surfaces of the sections of the sphere coincide with the toroidal coordinate surfaces). As demonstrated below, this solution can be used to evaluate the drag on spheres at different immersion depths in a gas/liquid interface using symmetry arguments.

3.2. Single Particle Straddling a Clean Interface at Arbitrary Immersion Depth

When the particle [either a sphere (**Figure 4**) or a body of revolution (**Figure 5**)] is straddling the fluid interface not symmetrically, but at a distance d above or below the surface (due to contact angles larger or smaller than $\pi/2$), both analytical and numerical solutions have been obtained. We discuss first the translation of spherical colloids along the surface of a gas/liquid interface ($\mu_2 = 0$ or $\beta = 0$) in the z-direction (**Figure 4*a***), where analytical solutions follow using the transform calculations that Zabarankin (2007) used for fused spheres (**Figure 5*c***). These solutions are symmetric with respect to the mirror plane ($z = 0$) of the fused spheres, and the shear stress is therefore equal to zero along this plane. Hence, the part of the symmetric solution below the mirror plane can represent the solution for a sphere at a gas/liquid interface and submerged to a depth $d = a \cos \eta_0$, where η_0 now represents the contact angle θ. Zabarankin (2007) obtained solutions for the drag for $0 < \eta_0 < \pi/2$ corresponding to immersion depths into the liquid from $d = 0$ (symmetrically straddling the interface) to $d = 1$ [completely emerged and just touching the interface ($z = 0$)]. The computed values are shown in **Figure 6**, where the drag coefficient $k_{\mathrm{D}}^{\mathrm{t}}$ is normalized by the Stokes drag coefficient in an infinite medium ($6\pi a \mu_1$).

When the sphere center lies above or below the interface ($-1 < d/a < 1$), solutions have been obtained using boundary integral (Pozrikidis 2007, Luo & Pozrikidis 2008), finite-difference (Danov et al. 1995, 2000), and finite-element methods (Das et al. 2018), and values of the drag coefficients from these simulations complete the range of d/a (see **Figure 6*a***). All of these calculations are for a slip coefficient of zero, except for the finite-element calculations, which are for a value of $\lambda/a = 0.01$ (which was shown to be within a few percent of $\lambda/a = 0$). The drag coefficient is found to increase monotonically with the immersion depth into the liquid phase until the particle becomes fully immersed ($d/a = 1$). This is as expected because as more of the surface area of the particle contacts the viscous liquid and less contacts the gas phase (which does not exert a viscous traction), a greater drag force is generated. For $d/a > 1$, Luo & Pozrikidis (2008) using boundary integral calculations and Davis et al. (1994) using eigenfunction expansions in bispherical and tangent sphere coordinates calculated $k_{\mathrm{D}}^{\mathrm{t}}$; these are also shown in **Figure 6**. As the particle locates further away from the interface ($d/a > 1$), the drag continues to increase monotonically. This is due to the influence of the gas/liquid interface on the flow around the particle, as well as the resultant viscous shear stress. In the gap between the particle surface and the fluid interface, viscous stresses are reduced, as the gas/liquid interface is mobile and velocity gradients are smaller. The further the particle moves into the liquid phase, the larger the gradients and the larger the drag, as the liquid in the gap presents a greater resistance to the particle's translation. For immersion

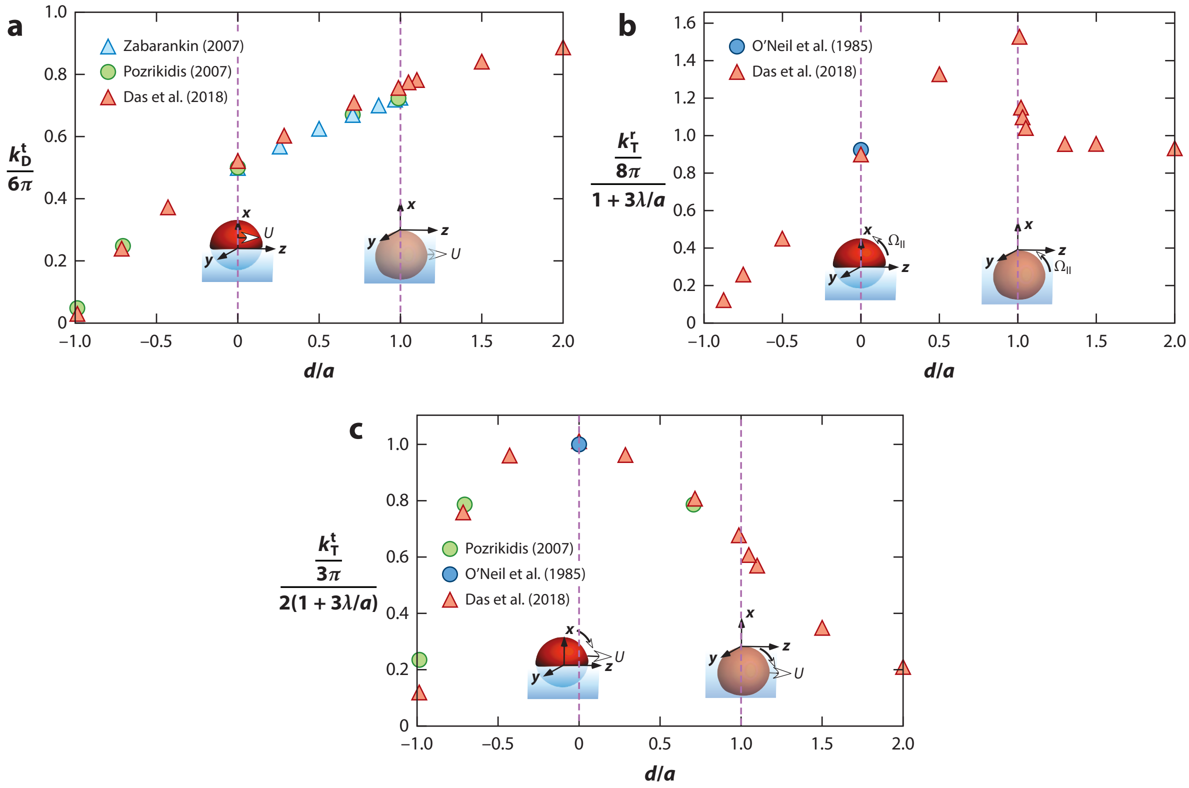

Figure 6

(*a*) Drag coefficient for translation k_D^t, (*b*) the resistive torque due to rotation k_T^r, and (*c*) the cross-coefficient (generated torque due to translation or drag due to rotation) as a function of immersion depth d/a for spheres on a clean fluid interface. The drag coefficient is normalized by the Stokes drag in a bulk liquid, the resistive torque coefficient is normalized by the value in the bulk, and the cross-coefficients are normalized by the value when the sphere straddles the interface, equally immersed in both phases.

depths d/a larger than $\mathcal{O}(10)$, k_D^t asymptotes to the Stokes drag coefficient $6\pi a\mu_1$ for translation in an infinite liquid as the effect of the fluid boundary disappears.

For rotation of a spherical particle about the axis passing through the sphere center and in the y-direction (**Figure 4*b***) at a gas/liquid interface, a slip coefficient λ has to be retained in order for the resistive torque on the particle due to rotation to remain finite (Section 3.1). As noted earlier, solutions for k_T^r have been obtained analytically by O'Neill et al. (1985) for half-immersion and different values of λ/a, and these were shown to diverge logarithmically in λ. Using a finite-element method, Das et al. (2018) obtained solutions for k_T^r for rotating spheres straddling the gas/liquid interface and further immersed in the liquid phase. These results, along with the calculation of O'Neill et al. (1985), are shown in **Figure 6*b*** for $\lambda/a = 0.01$ and $\beta = 0$, where the resistive torque k_T^r due to rotation is divided by the resistive torque coefficient when the colloid is completely immersed in the liquid, $8\pi\mu a^3/(1+3\lambda/a)$. The resistive torque increases with an increase in d/a, which corresponds to a decrease in contact angle. As the contact angle decreases, larger velocity gradients develop in the liquid cusp region between the sphere surface and the interface near the contact line because the cusp angle decreases. (Recall that the fluid interface is assumed to remain flat.) The increase in velocity gradients increases the resistive viscous shear on the rotating sphere

Review in Advance first posted on
November 18, 2021. (Changes may
still occur before final publication.)

and therefore the torque. At $d/a = 1$, the sphere is completely immersed in the liquid and just touching the interface. The resistive torque coefficient is finite, because the surface of the particle has finite slip ($\lambda/a = 0.01$). At this point where the rotating sphere breaches the interface, $k_{\mathrm{T}}^{\mathrm{r}}$ reaches its maximum value. As d/a increases further, the contact line is removed, and the effect of its cusp region on generating large resistive stresses disappears. For $d/a > 1$, $k_{\mathrm{T}}^{\mathrm{r}}$ decreases, as the resistive torque is only due to the viscous drag around the rotating particle. Davis et al. (1994) obtained analytical solutions for $d/a > 1$ for the case in which the colloid interface has zero slip. When the sphere is in the immediate vicinity of the interface ($1 < d/a < 1.1$), values of $k_{\mathrm{T}}^{\mathrm{r}}$ calculated by Davis et al. (1994) are larger than the $\lambda/a = 0.01$ coefficients in **Figure 6*b*** due to the surface slip, but they become nearly equal when the gap between the fluid interface and the surface of the particle becomes more than a few tenths of *a* because the slip coefficient is small. Larger slip coefficients were also investigated by Das et al. (2018), which led to reduced values of $k_{\mathrm{T}}^{\mathrm{r}}$.

As noted in **Figure 4*a***, a torque is generated by the translation of the particle in the z-direction due to the asymmetry in the tractions exerted on the particle from the bounding phases on either side of the interface. In the case of a gas/liquid interface, this asymmetry is very significant because the gas phase does not exert any tractions and acts to rotate the particle in a clockwise direction (there is a positive value for the cross-coefficient). The cross-coefficient $k_{\mathrm{T}}^{\mathrm{t}}$ describing the torque due to translation follows from symmetry arguments for $d = 0$ in Section 3.2 and, for a gas/liquid interface, is $k_{\mathrm{T}}^{\mathrm{t}}(d = 0, \beta = 0, \lambda/a) = (3\pi/2)[1/(1 + 3\lambda/a)]$. For other immersion depths, Pozrikidis (2007) and Das et al. (2018) have obtained solutions for spheres straddling different positions at the interface, and Davis et al. (1994) and Luo & Pozrikidis (2008) have obtained solutions for spheres below the interface. These results for the cross-coefficient are shown in **Figure 6*c*** as a function of d/a, normalized by the value when the sphere is half-immersed in the liquid with zero slip, $(3\pi/2)[1/(1 + 3\lambda/a)]$. As the sphere just breeches the interface from the gas side, the torque exerted on the colloid by translation is small since this torque arises from the liquid tractions and the contact area with the liquid is small. With further immersion, $k_{\mathrm{T}}^{\mathrm{t}}$ increases, reaching a maximum at half-immersion ($d/a = 0$) (where the asymmetry in the tractions across the sphere is the largest) and finally decreasing to zero as the particle becomes completely immersed in the liquid and located away from the interface. The other cross-coefficient, the normalized drag due to rotation ($k_{\mathrm{D}}^{\mathrm{r}}$), is found to be identical in prior studies as required by reciprocity, and its dependence on d/a follows also from the asymmetry arguments.

When the sphere translates in the z-direction along interface between two viscous liquids (i.e., $\beta \neq 0$), Pozrikidis (2007) has calculated the drag coefficient and the generated torque due to the translation. As expected, relative to the case when the phase above the interface is a gas, when the sphere straddles two viscous liquids with its center above the interface, the drag increases due to the increased viscous tractions. The tractions on both sides of the interface produce a drag in the $-z$-direction so that the drag coefficient is always of one sign. The torque coefficient displays more interesting behavior: For the gas/liquid interface, the generated torque is always in the clockwise direction (positive coefficient) due to the action of the tractions in the liquid phase beneath the interface, which generate a net torque in that direction. However, as the upper phase becomes more viscous, the tractions in that phase become more important and generate a torque in the counterclockwise direction. When the particle is positioned further in the upper phase and the viscosity contrast is large enough, the net generated torque becomes negative. When the bounding phases have equal viscosities, the cross-coefficient becomes antisymmetric and equal to zero for $d/a = 0$, as noted above for spheres half-immersed at an interface.

3.3. Single Particle Straddling an Amphiphilic Monolayer Interface or a Membrane Bilayer

Two applications in which the hydrodynamics of particles straddling an interface is important are the rotation/translation of proteins or other objects bound in biological membranes (Sickert et al. 2007) and the use of colloids as microrheology probes to measure surface viscosities (see, e.g., Elfring et al. 2016). Hydrodynamic studies must therefore include, in contrast to the cases discussed above in which the fluid interface was assumed to be clean and stress-free, the effects of an adsorbed amphiphilic monolayer or bilayer at the interface. In the literature, two fundamental models have been constructed to describe these effects: In the first, the particle is assumed to be embedded in a thin viscous layer of finite thickness representing the membrane or the monolayer. In the second, a monolayer or bilayer is assumed to be adsorbed at a fluid interface of zero thickness, and the particle, straddling the interface, protrudes into the surrounding phases. We focus attention on this latter model, as it follows the model constructs of the prior subsections, and we relate some of the results to the model in which the particle is embedded into a thin film. For the particle-protruding model, spheres and oblate ellipsoids have been studied. The monolayer or bilayer is modeled as a 2D surface fluid—typically a Newtonian surface fluid with surface stresses derived from resistance to interfacial shear and dilation, and an isotropic tension representing the surface pressure as a function of the surface concentration of the amphiphile. The concentration-dependent isotropic tension models the effect of Marangoni tractions on the fluid surface arising from gradients in the tension due to gradients in the surface concentration of the amphiphiles. The equation for the tangential stress balance at the interface is modified to includes the in-plane surface stress tensor $\mathbf{T}_s$:

$$\mathbf{n}_{(s)} \cdot [\![\boldsymbol{\tau}_{(s)i}]\!] \cdot \mathbf{t}_{(s)} + \mathbf{t}_{(s)} \cdot \nabla_s \cdot (\mathbf{T}_s) = 0, \tag{14.}$$

$$\mathbf{T}_s = -\Pi\,\mathbf{I} + \mu_s(\nabla \mathbf{v}_s + \nabla \mathbf{v}_s^{t}) + \kappa_s \nabla_s \cdot \mathbf{v}_s. \tag{15.}$$

Here μ_s and κ_s are the surface shear and area dilatational viscosities, respectively, which multiply the shear rate and the rate of area dilation $\nabla_s \cdot \mathbf{v}_s$; $\Pi(\Gamma) = \gamma_0 - \gamma(\Gamma)$ is the surface pressure, which is a function of the surface concentration Γ of the amphiphile as defined by an equation of state and the tension of the clean interface γ_0. The linear equation of state, representing small deviations from an equilibrium state with concentration Γ_{eq} and pressure Π_{eq}, is the simplest model for $\Pi(\Gamma)$ and is given by $\Pi(\Gamma) = \Pi_{eq} + \mathcal{E}\Gamma_{eq}(\Gamma - \Gamma_{eq})$, where $\mathcal{E} = (1/\Gamma_{eq})(\partial\Pi_{eq}/\partial\Gamma_{eq})$ is the Gibbs elasticity. The surface concentration is then solved with a surface mass balance.

The translational movement of a disk (radius R) along a flat fluid interface with an adsorbed amphiphilic monolayer or membrane has been examined by Stone & Ajdari (1998) and Sickert et al. (2007) for a surface incompressible layer and a gas/liquid interface with shear viscosity μ_s (**Figure 7*a***). These calculations were undertaken for a fluid interface a distance h above a flat surface with an intervening Newtonian liquid layer, and dual integral equations were solved to compute the drag coefficient k_D^t. For the case in which the surface viscosity is equal to zero and the particle radius is much smaller than the the liquid layer ($h/R \gg 1$), the calculated drag is $F_{(p)z} = -8\mu_1 RU$, which is 3/2 times larger than the result for a clean interface, $F_{(p)z} = -(16/3)\mu_1 RU$, and in agreement with the result of Fischer et al. (2006) that the surface incompressibility retards the translation of a particle embedded in the surface. Stone & Ajdari (1998) also presented results for finite values of the surface shear viscosity, expressed in terms of the dimensionless Boussinesq number $\mathcal{B} = \mu_s/(\mu_1 R)$, which characterizes the ratio of surface viscous to bulk viscous tractions on the translational motion. For $h/R \gg 1$, Stone & Ajdari (1998) showed that as $\mathcal{B}$ increases and surface viscous effects outscale bulk viscous effects, k_D^t increases and can

Review in Advance first posted on November 18, 2021. (Changes may still occur before final publication.)

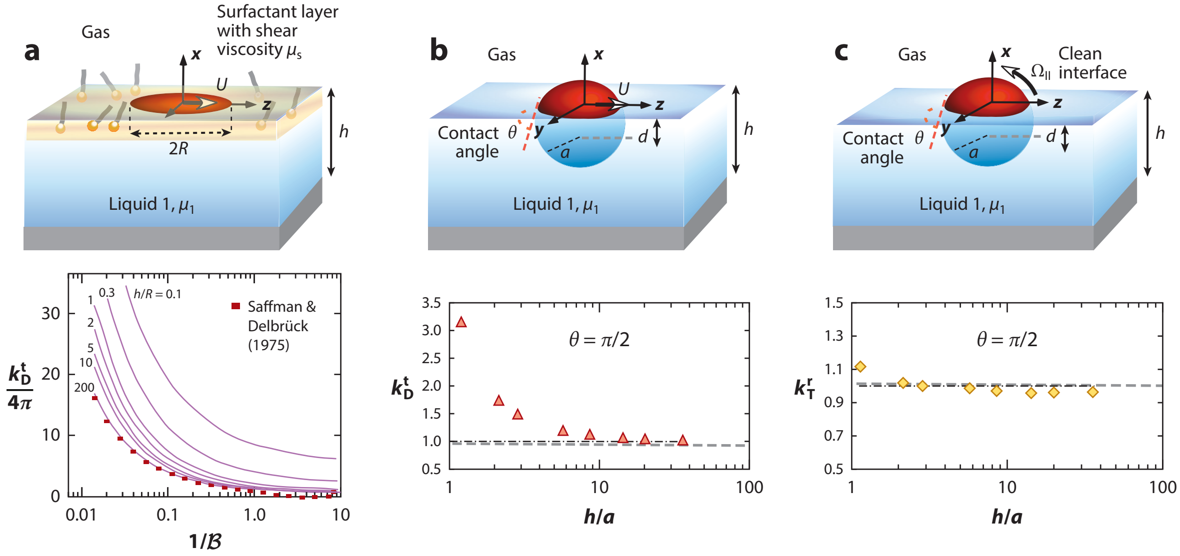

Figure 7

(*a*, *Top*) A disk of radius R embedded in a fluid interface with a surfactant monolayer or bilayer of shear viscosity μ_s, translating at velocity $U\mathbf{e}_z$ atop a film of thickness h and viscosity μ_1. (*Bottom*) Translational drag coefficient k_D^t plotted against the dimensionless Boussinesq number $\mathcal{B} = \mu_s/(\mu_1 R)$. Panel *a* adapted with permission from Stone & Ajdari (1998). (*b*,*c*, *Top row*) Sphere of radius a, half-immersed in a liquid phase of thickness h and viscosity μ_1, (*b*) translating at velocity $U\mathbf{e}_z$ or (*c*) rotating at angular velocity $\Omega_\parallel \mathbf{e}_y$. The bottom row shows (*b*) the translational drag coefficient and (*c*) the rotational resistive torque coefficient for these respective cases, divided by the values when the sphere is completely immersed a semiinfinite liquid phase, plotted against h/a. Panels *b* and *c* adapted with permission from Das et al. (2018).

be an order of magnitude larger than the value for for zero surface viscosity. The calculations of Stone & Ajdari (1998) are plotted in **Figure 7*a***.

Saffman & Delbrück (1975) and Saffman (1976) calculated the translational drag of a cylinder of radius R and thickness h moving in a thin, planar film of the same thickness and viscosity μ_f, which defines an effective surface viscosity $\mu_s = h\mu_f$. The film is bounded by semiinfinite liquid phases with equal Newtonian viscosities μ_1, or (by symmetry) by gas and liquid phases defining a Boussinesq number $\mathcal{B} = \mu_s/(\mu_1 R) = (h\mu_f)/(\mu_1 R)$. In the limit in which the bounding phase viscosities are smaller than the film phase, $\mathcal{B} \gg 1$, Saffman & Delbrück (1975) developed an asymptotic expression for the drag coefficient in the limit in which the cylinder can be considered a point force:

$$F_{(p)z}^{\text{disk in film}} = -\frac{4\pi R\mathcal{B}}{\ln(2\mathcal{B}) - \gamma}U \qquad (\mathcal{B} \gg 1).$$

In **Figure 7*a***, the Saffman & Delbrück (1975) result is plotted and is shown to agree with the exact solution of Stone & Ajdari (1998) in the limit of large Boussinesq number and sufficiently large h/R. This expression was improved for a larger range of $\mathcal{B}$ by Hughes et al. (1981). Relaxation of the surface incompressibility limit and inclusion of Marangoni tractions driven by gradients in the amphiphile concentration created by the translation were examined by Dimova et al. (2000) and, more completely, by Pourali et al. (2021).

Fischer et al. (2006) examined the translation of a sphere through a monolayer on a flat gas/liquid interface that was assumed to be two-dimensionally incompressible ($\nabla_s \cdot \mathbf{v}_s = 0$), and obtained solutions for the translational drag coefficient k_D^t (assuming a zero-slip coefficient) as a function of the immersion depth d/a. Adsorbed monolayers of amphiphiles have high

Review in Advance first posted on November 18, 2021. (Changes may still occur before final publication.)

elasticities (or dilatational viscosities), which lead to nearly incompressible behavior; therefore, the limit $\nabla_s \cdot \mathbf{v}_s = 0$ can be viewed as characterizing how strongly the monolayers or membranes affect the particle translation. For the case in which the shear viscosity of the membrane is equal to zero ($\mu_s = 0$), when compared to the values for a clean interface, the results of Fischer et al. (2006) make clear that the restriction of incompressibility limits the mobility of the particle immersed in the monolayer/membrane and increases the drag coefficient. Values for the cross-coefficient $k^{\mathrm{t}}_{\mathrm{T}}$ were also calculated and followed the same trend as shown in **Figure 5**, except that the coefficient values are larger for each value of d/a. As with the case for the translation of a circular disk along a flat incompressible fluid surface, the inclusion of shear viscosity increases the drag; in the limit of large Boussinesq number, where the shear viscosity dominates bulk viscosity, Fischer et al. (2006) found

$$F_{(\mathrm{p})z} = -\frac{4\pi R\mathcal{B}}{\ln\left(\frac{\mathcal{B}}{\sin\theta}\right) - \gamma}U \qquad (\mathcal{B} \gg 1),$$

where θ is the contact angle. This expression agrees with the Saffman expression (Saffman & Delbrück 1975, Saffman 1976) except for the term $2\mathcal{B}$ in the logarithm is replaced by $\mathcal{B}/\sin\theta$, accounting for the fact that the sphere is protruding into the liquid while the disk is embedded entirely in the film. The studies of Fischer et al. (2006) have been extended by Masoud & Stone (2019) and Stone & Masoud (2015) for the case of spheres and oblate spheroids moving over a gas/liquid interface with an adsorbed monolayer or bilayer in which these objects only protrude into the liquid phase a distance h_{p} that is small relative to the major axis of the ellipsoid or the radius of the sphere.

The above sections discuss the hydrodynamics of a single colloid on a planar fluid interface that is bounded by either two semiinfinite liquid phases, or a gas and a semiinfinite liquid. If the interface is next to a solid surface, then the particle motion will be affected by the interaction with the surface as mediated by the intervening liquid. This problem has been addressed for straddling spheres on a clean interface by Das et al. (2018) (**Figure 7*b*,*c***) or for disks by Stone & Ajdari (1998) (**Figure 7*a***), where the fluid interface has an adsorbed amphiphilic layer or bilayer membrane. In both studies the interface is bounded by a gas phase and a liquid layer atop a solid surface. In **Figure 7*b*** the drag coefficient is plotted as a function of the thickness of the underlying liquid layer for a sphere straddling the interface with a contact angle of $\pi/2$. The coefficient is normalized by the drag coefficient when the solid surface is infinitely far from the interface (3π), and it is clear that the presence of the wall increases the drag as the underlying liquid layer exerts a larger viscous resistance due to the no-slip condition at the wall creating a larger velocity gradient in the layer. For a rotating sphere half-immersed in the liquid, the coefficient of resistive torque does not show a large increase with decreasing layer thickness (**Figure 7*c***), as resistance generated by the large gradients near the contact line is the dominant contribution to the resistive torque. For a disk translating edgewise on a gas/liquid interface with a amphiphilic monolayer or bilayer, the drag similarly increases with decreasing layer thickness, as shown in **Figure 7*a*** for a fixed value of the monolayer shear viscosity (Boussinesq number). Note importantly that as $\mathcal{B}$ increases, the retarding effect of the surface shear viscosity becomes dominant, and a decrease in the layer thickness leads to a small increase in the drag coefficient.

3.4. Pairwise Interactions of Colloids Straddling a Fluid Interface

The above sections make clear that the hydrodynamics of a single particle straddling a fluid interface in Stokes flow has been studied in some detail. The hydrodynamic interactions of multiple particles has not been examined as extensively, particularly on a fundamental level that begins with pairwise interactions. For colloids completely immersed in a bulk phase in Stokes flow, these pairwise interactions are well understood (e.g., Jeffrey & Onishi 1984). In particular, for pairs of

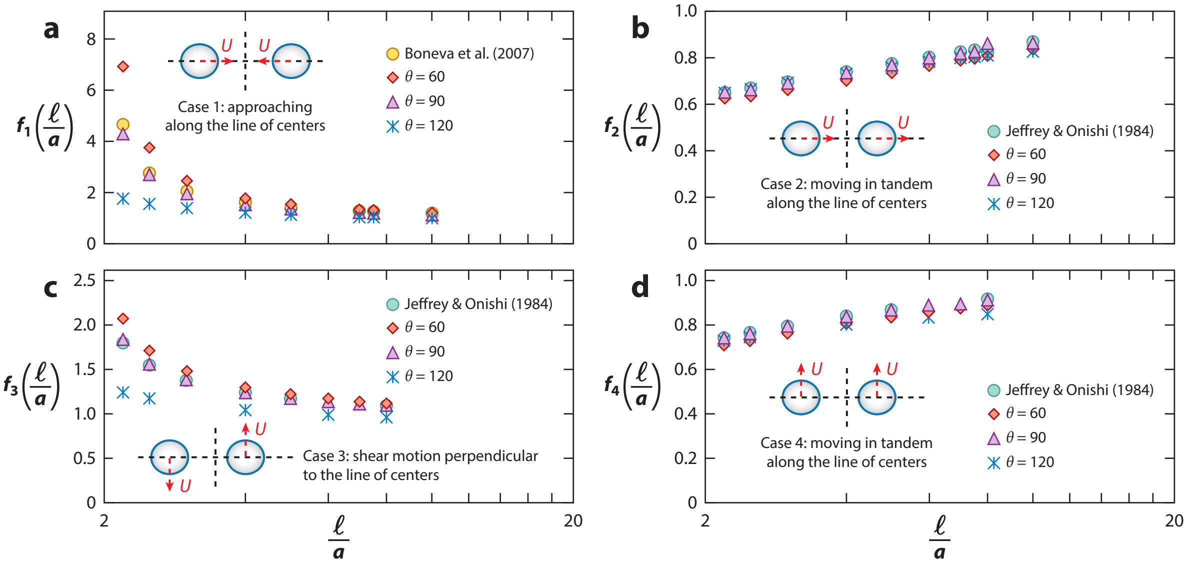

Figure 8

Drag coefficients (*a*) f_1, (*b*) f_2, (*c*) f_3, and (*d*) f_4 for the canonical pairwise motions of two spheres of radius a on a fluid interface as a function of immersion depth (contact angle θ) and center-to-center separation distance ℓ. Cases 1 and 2 (*a*,*b*) are motions parallel to the line of centers connecting the spheres, and cases 3 and 4 (*c*,*d*) are motions perpendicular to the line of centers. The drag coefficients are scaled by the coefficient of an isolated sphere at that immersion depth, $k_{\mathrm{D}}^{\mathrm{t}}(d/a,\ \beta = 0)$. Figure adapted with permission from Das et al. (2021).

spheres rotating and translating relative to one another in a liquid phase at a separation ℓ, the drag and resistive torque coefficients (and the corresponding cross-coefficients) have been calculated by analytical and numerical methods. For a pair of spherical colloids straddling a flat gas/liquid interface, each at an immersion depth d, Das et al. (2021) have computed the drag coefficients for the spheres traveling in tandem along [case 2; $f_2(d/a, \ell/a)$] or perpendicular to [case 4; $f_4(d/a, \ell/a)$] their line of centers, as well as for spheres with oppositely directed motion along [case 1; $f_1(d/a, \ell/a)$] or perpendicular to [case 3; ($f_2(d/a, \ell/a)$] their line of centers (**Figure 8**). The drag coefficients, scaled by the coefficient of an isolated particle at that immersion depth, $k_{\mathrm{D}}^{\mathrm{t}}(d/a,\ \beta = 0)$, are plotted in **Figure 8** as a function of the separation distance between the spheres for different immersion depths.

For in-tandem motions (**Figure 8*b*,*d***) the coefficients increase with a decrease in the separation distance and collapse into one curve for all immersion depths. These collapsed curves coincide with the drag coefficients computed by Jeffrey & Onishi (1984) (normalized by the Stokes drag of an isolated particle in an infinite medium) for two particles moving in tandem and completely immersed in the liquid either along the line of centers or perpendicular to line of centers. These calculations verify a simple rule for calculating the in-tandem coefficients at a flat gas/liquid interface:

$$\frac{\hat{f}_i(d/a, \ell/a)}{k_{\mathrm{D}}^{\mathrm{t}}(d/a, \beta = 0)} \approx \frac{\hat{f}_{i,\infty}(\ell/a)}{6\pi} \qquad (i = 2, 4), \qquad 16.$$

where $\hat{f}_{i,\infty}(\ell/a)$ and $\hat{f}_i(d/a, \ell/a)$ are drag coefficients in an infinite medium and on the surface simply nondimensionalized by μa. For oppositely direct motions (**Figure 8*a*,*c***), the scaled resistance coefficients increase with a decrease in separation distance but do not collapse for different immersion depths to the corresponding normalized drag coefficient curves for particles in an infinite medium. When the particle preferentially wets the liquid (for contact angles less than $\pi/2$), the scaled resistance increases without bound as the separation distance tends to zero because of the unbounded increase in the lubrication forces. For oppositely directed motions in which the particle resides predominantly in the gas phase, the scaled resistance tends to a finite value at zero separation since upon contact fluid remains entrained in the gap between the particles. Only for neutral wetting do the scaled resistances collapse to the curves for particles immersed in an infinite medium, due to the symmetry of the motion.

3.5. Hydrodynamic Interactions of Multiple Particles at a Fluid Interface

Several studies have examined the hydrodynamic interaction of multiple particles on a flat interface. Dehghani et al. (2017) and Barman & Christopher (2016) studied a surface shear (Couette) flow, with a 2D Stokesian dynamics simulation that included the interparticle forces of capillary and electrostatic repulsion. This work was extended to study aggregation in the absence of an imposed flow (Dehghani & Christopher 2019; Rahman et al. 2019a,b). Pairwise hydrodynamic interactions were accounted for by Equation 16. The drag on a planar array of immobile colloids on a gas/liquid interface ($d/a = 0$) was studied by Vidal & Botto (2017). They placed the array, fully immersed, at the midplane of a channel with a shear flow and used the symmetry to obtain the drag on the particles at an air/liquid interface (half the fully immersed drag). Discrete-element and Brownian dynamics simulations (see Nishikawa et al. 2003, 2006; Fujita et al. 2004; Millett & Wang 2011; Uzi et al. 2016) have simulated the self-organization, with detailed accounting using diffuse interface theory, of the capillary attraction and electrostatic interaction forces. Particles that are magnetized by an external magnetic field and adsorbed at a gas/liquid interface (or just below the interface) have been a model system for understanding 2D particle dynamics (e.g., Zahn et al. 1997; Rinn et al. 1999; Zahn & Maret 1999; Kollmann et al. 2002; Löwen et al. 2005; Vandewalle et al. 2012, 2013; Lumay et al. 2013; Darras et al. 2018; Du et al. 2018; Hilou et al. 2018).

3.6. Molecular Dynamics Simulations of the Translation of Nanoparticles on a Fluid Interface

The MD framework for studying the motion of nanoparticles on a vapor/liquid surface was discussed in Section 2. The liquid was composed of tetramers and the nanoparticle was a sphere of atoms cut from a cubic lattice. The atoms all interacted by LJ potentials with the interaction constant c_{12} describing the attraction of the nanoparticle atoms to the tetrameric liquid atoms. The larger this interaction, the more wettable is the nanoparticle to the liquid and, at equilibrium, the deeper is the immersion of the nanoparticle into the liquid side of the interface (smaller contact angle). Using this model, Koplik & Maldarelli (2017) obtained the drag coefficient using three different methods. In the first, the diffusive motion of the nanoparticle along the surface was observed in time, and from the mean square displacement, the diffusion coefficient was calculated. From the diffusion coefficient and the Stokes–Einstein equation, the drag coefficient on the particle was obtained. Alternatively, the velocity autocorrelation for this diffusive motion was measured, and the diffusivity and drag was computed. Third, the nanoparticle was dragged at constant velocity along the interface (at its equilibrium immersion depth), and the force was measured and averaged to compute the drag coefficient. In all these simulations, the particle was allowed to freely rotate. A final simulation was undertaken in which the particle was moved at a constant velocity along the surface, but the rotation was suppressed and the force and drag coefficient were measured.

The drag coefficients obtained by these methods are plotted as a function of the interaction energy c_{12} in **Figure 9*a***, where the drag coefficients are divided by the drag on the nanoparticle in

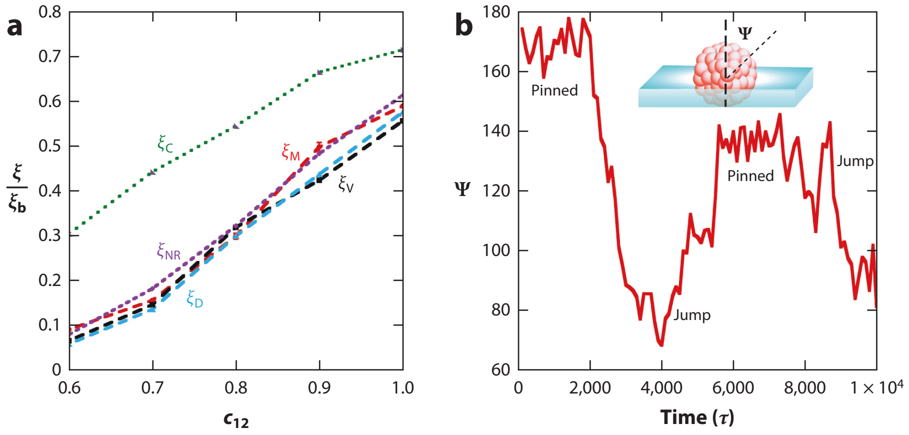

Figure 9

(*a*) Drag coefficients normalized by the bulk Stokes drag ξ_b as a function of the interaction parameter c_{12}: ξ_C is the drag coefficient from a continuum study for a no-slip sphere (**Figure 6**), ξ_M is the drag coefficient calculated from the mean square displacement of diffusive measurements using the Stokes–Einstein relation, ξ_V is the drag coefficient obtained from the velocity autocorrelation of diffusing spheres, ξ_D is the drag coefficient directly measured for a freely rotating sphere dragged along the interface, and ξ_{NR} is the drag coefficient directly measured for a nonrotating pulled sphere. (*b*) Rotation angle Ψ as a function of nondimensional time τ as a particle diffuses along the surface. Figure adapted with permission from Koplik & Maldarelli (2017).

a bulk medium. This drag was also obtained by MD simulation of a nanoparticle diffusing along or being pulled at a constant velocity in the tetramer liquid and away from the interface. The value obtained was in good agreement with the Stokes drag. From **Figure 9*a***, it is clear that the coefficients computed by the different methods are in agreement and demonstrate that the greater the immersion depth, the larger the drag coefficient, in agreement with the continuum calculations (**Figure 6**). **Figure 9** also plots the relative drag coefficients from the continuum calculations. The MD drag coefficients are systematically smaller at each immersion depth, a result that can be attributed to the fact that the nanoparticles translate through an interface of reduced density and interfacial traction (**Figure 5**). The MD simulations also provide a unique perspective on the rotation of the nanoparticle and provide insight into the effect of roughness, as the nanoparticle surface is not smooth. In **Figure 9*b***, the angle Ψ between a fixed line through the nanoparticle and the interface is plotted as a function of time for a particle diffusing along the surface for $c_{12} = 0.7$. It is clear that the rotation is not completely free, but executes stick–slip motions due to the surface roughness.

4. EXPERIMENTAL MEASUREMENTS OF DRAG COEFFICIENTS FOR PARTICLES MOVING ALONG A SURFACE

4.1. Isolated Particles

Some experimental work has been done on measuring the drag force on isolated spherical colloids forced to move along a surface by capillary or magnetic forces by equating the actuating forces to the Stokes drag. To compare the drag to the theoretical predictions of **Figure 6**, one also needs the contact angle or the immersion depth, and these measurements were discussed above (Section 2). For single spheres, Petkov et al. (1995) measured the velocity of glass particles (a few hundred micrometers in radius) that translated up an air/water meniscus. Contact angles were obtained by visualization. A trajectory was simulated as a function of time and comparison with the experimental data yielded the Stokes drag, which was in very good agreement with the theoretical predictions given by **Figure 6**. Vassileva et al. (2005) measured the drag on single glass particles a few hundred micrometers in radius moving up a meniscus at the pentadecane/glycerol-water interface with matched viscosities. The contact angles were measured by direct visualization. Comparison of the experimental trajectories with the simulations yielded a value for the drag coefficient slightly larger than that of the theoretical prediction. Ally & Amirfazli (2010) used polystyrene particles (a few micrometers in radius) embedded with magnetite floating on planar air/water and air/silicone oil interfaces. Ally & Amirfazli (2010) applied a measured magnetic field along the surface to move the particles, and contact angles were measured using film trapping and interferometry. The experimental trajectories were in good agreement with the simulation values using the drag coefficients in **Figure 6**.

Experiments on smaller spherical colloids (100 nm–1 μm in diameter) in which the diffusivity is first measured directly by tracking the fluctuating position of the particle due to Brownian motion, and then computing the drag coefficient from the Stokes–Einstein relation, do not systematically agree with theoretical predictions. For hydrophobic particles at the decalin (oil)/water interface, Peng et al. (2008) obtained a diffusion coefficient approximately equal to the value in the bulk oil phase, noting that this result followed from the almost complete immersion of the colloid in the oil. For partially wetting particles at the silicone oil/water interface, Du et al. (2012) obtained a value for the diffusion coefficient that was between the bulk phase diffusivities, as would be anticipated. Sickert et al. (2007) and Sickert & Rondelez (2003) have demonstrated that the surface diffusivity of particles at the air/water interface (for small contact angles) is larger than it is in the bulk (due to the smaller drag coefficient) but smaller than the continuum prediction. However, other experiments have shown anomalous behavior for the surface drag coefficient: Gehring & Fischer (2011) studied charged spherical nanoparticles (of the order 100 nm) at the air/water interface and obtained drag coefficients larger than the theoretical bulk value. They attributed this result to surface viscous forces due to the presence of surfactants on the surface. For large contact angles of hydrophobic particles at the air/water surface, Boniello et al. (2015) showed that the surface drag coefficient was larger than the bulk value [see Radoev et al. (1992), Chen & Tong (2008), Dhar et al. (2008), Maestro et al. (2011), and Samaniuk & Vermant (2014), which also report anomalous behavior]. Dissipation of energy at the contact line due to thermal fluctuations has been reported as the reason for this anomalous behavior (Boniello et al. 2015, Villa et al. 2020).

4.2. Pairwise Interactions of Particles on a Surface

Vassileva et al. (2005) located two submillimeter-sized glass spheres a few capillary lengths close to one another on a pentadecane/glycerol-water interface with matching bulk viscosities, and measured the decrease in separation due to capillary attraction. Contact angles were measured by direct visualization. A theoretical prediction was constructed that accounted for the hydrodynamic interaction between the particles using Equation 16, and good agreement was obtained. Two particle capillary attraction investigations were also undertaken by Dalbe et al. (2011) using millimeter-sized polyethylene and nylon spheres at the air/glycerol-water interface with contact angles measured by visual inspection. Using Equation 16, the authors simulated the approach trajectory and found qualitative agreement, presumably because they did not account for the dependence of the single-particle drag coefficient on the immersion depth. Boneva et al. (2007, 2009) studied two hydrophobized glass colloids (charged and uncharged) a few hundred micrometers in radius interacting by electrostatic and capillary attractive forces at a tetradecane/water interface, and measured contact angles directly by visualization. They observed an attraction and simulated the trajectory using Equation 16, but with a single-particle drag coefficient obtained by a wetted area approximation. Boneva et al. (2007, 2009) observed reasonable agreement for uncharged particles, although the experimental drag exceeded the theoretical prediction. For the charged particles, the agreement was not as good, a consequence apparently of the neglect of the electrostatic component of the interaction in the theoretical simulation. Similarly, Dani et al. (2015) measured the gravity-induced capillary attraction of millimeter-sized Teflon$^{\text{TM}}$ spheres at an oil/water interface and simulated the trajectory of the approaching spheres using Equation 16 and direct visualization for contact angle measurements. They found very good agreement with the experiments when the effect of the immersion depth on the single particle drag coefficient was taken into account.

5. PERSPECTIVE AND FUTURE DIRECTIONS

This review makes clear that in describing the hydrodynamic motion of colloids straddling a fluid interface, the analysis of the motion for Stokes flows and isolated particles is fairly well developed, and experiments on the translational motion agree with the theoretical predictions. The important exceptions are the experiments that obtain the (translational) drag coefficient by measuring the diffusion coefficient of the particles as they fluctuate on an air/water interface by Brownian forces. These experiments obtain the drag coefficient using the Stokes–Einstein equation, and lead to the anomalous result that the drag coefficient is larger when the colloid is on the surface than when it is in the bulk liquid. Pairwise interaction of particles in Stokes flow on a surface is also complete (at least for translational motions), but the simulations have not been fully tested experimentally because systematic experiments have not been undertaken on the capillary attraction of colloids while varying the particle immersion depth. Stokesian dynamics simulations for assemblies of particles on a surface have begun, and these studies can be used to understand microstructure formation and assembly under the influence of different applied in-plane forces. MD simulations have only begun to examine the hydrodynamics of nanoparticles moving along the surface. With this summary, several areas for new research become apparent, as outlined below.

FUTURE ISSUES

1. Molecular dynamics (MD) simulations allow the hydrodynamic motion of colloids straddling a fluid interface to be studied on the nanoscale, and can offer insights into how the particle surface topology and chemical heterogeneity affects the rotational mobility of the particle. Very little work has been done in this area, and continuum calculations are difficult to undertake (see Dörr & Hardt 2015). MD simulations provide an easier route to understand these effects (Koplik & Maldarelli 2017) and efforts should be made in this direction.
2. Most studies, both continuum and MD, examine the case of clean fluid interfaces. The exceptions are studies that examine particles moving along a fluid surface with an amphiphilic monolayer or bilayer (e.g., Stone & Masoud 2015, Sickert et al. 2007). These studies assume that the surface is incompressible and focus on the effect of the surface shear viscosity. While this modeling is most relevant to biological systems, surfactant monolayers are not always incompressible, and detailed attention has not been paid to the Marangoni forces developing when the surface is compressible. Some studies in this direction have been undertaken for translational motion driven by an external force,

including the influence of surface viscous and Marangoni effects (Elfring et al. 2016, Pourali et al. 2021), and for active colloids at an interface driven by Marangoni gradients (e.g., Vandadi et al. 2017, Dietrich et al. 2020), but more detailed studies using realistic descriptions of the surface elasticity should be encouraged.

3. The disconnect between theory and experiment with regard to the calculated drag coefficients for micrometer-sized particles as obtained by measurements of their diffusion coefficient needs to be understood. MD simulations are a natural choice to understand how thermal fluctuations at the contact line can give rise to an enhanced drag, which has been posited as the reason for this disconnect, and offer a promising route for explaining this anomalous behavior.

DISCLOSURE STATEMENT

The authors are not aware of any biases that might be perceived as affecting the objectivity of this review.

ACKNOWLEDGMENTS

The authors acknowledge the support of the National Science Foundation through grants CBET-1805554 and CBET-1929502.

LITERATURE CITED

Ally J, Amirfazli A. 2010. Magnetophoretic measurement of the drag force on partially immersed microparticles at air–liquid interfaces. *Colloids Surf. A* 360(1):120–28

Ballard N, Law AD, Bon SA. 2019. Colloidal particles at fluid interfaces: behaviour of isolated particles. *Soft Matter* 15(6):1186–99

Barman S, Christopher GF. 2016. Role of capillarity and microstructure on interfacial viscoelasticity of particle laden interfaces. *J. Rheol.* 60(1):35–45

Binks BP. 2002. Solid-stabilised emulsions and foams. *Curr. Opin. Colloid Interface Sci.* 7(1–2):21–41

Binks BP, Horozov TS, eds. 2006. *Colloidal Particles at Liquid Interfaces*. Cambridge, UK: Cambridge Univ. Press

Blanc C, Fedorenko D, Gross M, In M, Abkarian M, et al. 2013. Capillary force on a micrometric sphere trapped at a fluid interface exhibiting arbitrary curvature gradients. *Phys. Rev. Lett.* 111(5):058302

Bleibel J, Dominiguez A, Oettel M. 2013. Colloidal particles at fluid interfaces: effective interactions, dynamics and gravitation-like instability. *Eur. Phys. J. Spec. Top.* 222:3071–87

Boneva MP, Christov NC, Danov KD, Kralchevsky PA. 2007. Effect of electric-field-induced capillary attraction on the motion of particles at an oil–water interface. *Phys. Chem. Chem. Phys.* 9(48):6371–84

Boneva MP, Danov KD, Christov NC, Kralchevsky PA. 2009. Attraction between particles at a liquid interface due to the interplay of gravity- and electric-field-induced interfacial deformations. *Langmuir* 25(16):9129–39

Boniello G, Blanc C, Fedorenko D, Medfai M, Mbarek NB, et al. 2015. Brownian diffusion of a partially wetted colloid. *Nat. Mater.* 14(9):908–11

Bouzigues CI, Tabeling P, Bocquet L. 2008. Nanofluidics in the Debye layer at hydrophilic and hydrophobic surfaces. *Phys. Rev. Lett.* 101:114503

Bowles A, Honig C, Ducker W. 2011. No-slip boundary condition for weak solid–liquid interactions. *J. Phys. Chem. C* 115:8613–21

Bresme F, Oettel M. 2007. Nanoparticles at fluid interfaces. *J. Phys. Condens. Matter* 19:413101

Burmeister F, Schafle C, Matthes T, Bahmisch M, Boneberg J, Leiderer P. 1997. Colloid monolayers as versatile lithographic masks. *Langmuir* 13(11):2983–87

Chan DYC, Henry JH Jr., White LR. 1981. The interaction of colloidal particles collected at fluid interfaces. *J. Colloid Interface Sci.* 79(2):410–18

Chen W, Tan S, Huang Z, Ng TK, Ford W, Tong P. 2006. Measured long-range attractive interaction between charged polystyrene latex spheres at a water-air interface. *Phys. Rev. E* 74:021406

Chen W, Tan S, Ng TK, Ford WT, Tong P. 2005. Long-ranged attraction between charged polystyrene spheres at aqueous interfaces. *Phys. Rev. Lett.* 95:218301

Chen W, Tong P. 2008. Short-time self-diffusion of weakly charged silica spheres at aqueous interfaces. *EPL* 84:28003

Cheng S, Grest G. 2012. Structure and diffusion of nanoparticle monolayers floating at liquid/vapor interfaces: a molecular dynamics study. *J. Chem. Phys.* 136:214702

Colosqui CE, Morris JF, Koplik J. 2013. Colloidal adsorption at fluid interfaces: regime crossover from fast relaxation to physical aging. *Phys. Rev. Lett.* 111(2):028302

Cottin-Bizonne C, Cross B, Steinberger A, Charlaix E. 2005. Boundary slip on smooth hydrophobic surfaces: intrinsic effects and possible artifacts. *Phys. Rev. Lett.* 94:056102

Dalbe MJ, Cosic D, Berhanu M, Kudrolli A. 2011. Aggregation of frictional particles due to capillary attraction. *Phys. Rev. E* 83(5):051403

Dani A, Keiser G, Yeganeh M, Maldarelli C. 2015. Hydrodynamics of particles at an oil–water interface. *Langmuir* 31(49):13290–302

Danov KD, Aust R, Durst F, Lange U. 1995. Influence of the surface viscosity on the drag and torque coefficients of a solid particle in a thin liquid layer. *Chem. Eng. Sci.* 50:263–77

Danov KD, Dimova R, Pouligny B. 2000. Viscous drag of a solid sphere straddling a spherical or flat surface. *Phys. Fluids* 12:2711–22

Danov KD, Kralchevsky PA. 2006. Electric forces induced by a charged colloid particle attached to the water–nonpolar fluid interface. *J. Colloid Interface Sci.* 298(1):213–31

Danov KD, Kralchevsky PA. 2010a. Capillary forces between particles at a liquid interface: general theoretical approach and interactions between capillary multipoles. *Adv. Colloid Interface Sci.* 154(1–2):91–103

Danov KD, Kralchevsky PA. 2010b. Interaction between like-charged particles at a liquid surface: electrostatic repulsion versus capillary attraction. *J. Colloid Interface Sci.* 345:505–14

Darras A, Mignolet F, Vandewalle N, Lumay G. 2018. Remote-controlled deposit of superparamagnetic coloidal droplets. *Phys. Rev. E* 98(6):062608

Das S, Koplik J, Farinato R, Nagaraj D, Maldarelli C, Somasundaran P. 2018. The translational and rotational dynamics of a colloid moving along the air-liquid interface of a thin film. *Sci. Rep.* 8:8910

Das S, Koplik J, Somasundaran P, Maldarelli C. 2021. Pairwise hydrodynamic interactions of spherical colloids at a gas-liquid interface. *J. Fluid Mech.* 915:A99

Davis AM, Kezirian M, Brenner H. 1994. On the Stokes-Einstein model of surface diffusion along solid surfaces: slip boundary conditions. *J. Colloid Interface Sci.* 165:129–40

Dehghani NL, Christopher GF. 2019. 2D Stokesian simulation of particle aggregation at quiescent air/oil-water interfaces. *J. Colloid Interface Sci.* 553:259–68

Dehghani NL, Khare R, Christopher GF. 2017. 2D Stokesian approach to modeling flow induced deformation of particle laden interfaces. *Langmuir* 34(3):904–16

Denkov ND, Velev O, Kralchevsky PA, Ivanov IB, Yoshimura H, Nagayama K. 1992. Mechanism of formation of two dimensional crystals from latex particles on substrates. *Langmuir* 8:3183–90

Denkov ND, Velev O, Kralchevsky PA, Ivanov IB, Yoshimura H, Nagayama K. 1993. Two dimensional crystallization. *Nature* 361:26

Deshmukh OS, van den Ende D, Stuart MC, Mugele F, Duits MH. 2015. Hard and soft colloids at fluid interfaces: adsorption, interactions, assembly & rheology. *Adv. Colloid Interface Sci.* 222:215–27

Dhar P, Prasad V, Weeks E, Bohlein T, Fischer TM. 2008. Immersion of charged nanoparticles in a salt solution/air interface. *Phys. Chem. B* 112:9565–67

Dietrich K, Jaensson N, Buttinoni I, Volpe G, Isa L. 2020. Microscale Marangoni surfers. *Phys. Rev. Lett.* 125(9):098001

Dimova R, Danov K, Pouligny B, Ivanov IB. 2000. Drag of a solid particle trapped in a thin film or at an interface: influence of surface viscosity and elasticity. *J. Colloid Interface Sci.* 226(1):35–43

Dominguez A, Oettel M, Dietrich S. 2007. Theory of capillary-induced interactions beyond the superposition approximation. *J. Chem. Phys.* 127:204706

Dörr A, Hardt S. 2015. Driven particles at fluid interfaces acting as capillary dipoles. *J. Fluid Mech.* 770:5–26

Dörr A, Hardt S, Masoud H, Stone HA. 2016. Drag and diffusion coefficients of a spherical particle attached to a fluid–fluid interface. *J. Fluid Mech.* 790:607–18

Du D, Hilou E, Biswal SL. 2018. Reconfigurable paramagnetic microswimmers: Brownian motion affects non-reciprocal actuation. *Soft Matter* 14(18):3463–70

Du K, Liddle J, Berglund A. 2012. Three-dimensional real-time tracking of nanoparticles at an oil-water interface. *Langmuir* 28:9181–88

Elfring GJ, Leal LG, Squires TM. 2016. Surface viscosity and marangoni stresses at surfactant laden interfaces. *J. Fluid Mech.* 792:712–39

Fischer TM, Dhar P, Heinig P. 2006. The viscous drag of spheres and filaments moving in membranes or monolayers. *J. Fluid Mech.* 558:451–75

Foret L, Wurger A. 2004. Electric-field induced capillary interaction of charged particles at a polar interface. *Phys. Rev. Lett.* 92:058302

Fournier J, Galatola P. 2002. Anisotropic capillary interactions and jamming of colloidal particles trapped at a liquid-fluid interface. *Phys. Rev. E* 65:031601

Fujita M, Nishikawa H, Okubo T, Yamaguchi Y. 2004. Multiscale simulation of two-dimensional self-organization of nanoparticles in liquid film. *Jpn. J. Appl. Phys.* 43(7R):4434–42

Galatola P, Fournier J. 2014. Capillary force acting on a colloidal particle floating on a deformed interface. *Soft Matter* 10:2197–212

Gehring T, Fischer TM. 2011. Diffusion of nanoparticles at an air/water interface is not invariant under a reversal of the particle charges. *J. Phys. Chem. C* 115:23677–81

Ghezzi F, Earnshaw J, Finnis M, McCluney M. 2001. Pattern formation in colloidal monolayers at the air–water interface. *J. Colloid Interface Sci.* 238(2):433–46

Guzmán E, Abelenda-Núñez I, Maestro A, Ortega F, Santamaria A, Rubio RG. 2021. Particle-laden fluid/fluid interfaces: physico-chemical foundations. *J. Phys. Condens. Matter* 33:333001

Hadjinski A, Dimova R, Denkov N, Ivanov I, Borwanker R. 1996. Film trapping technique: precose method for three phase contact angle determnation of solid and fluid particles of micrometer size. *Langmuir* 12:6665–75

Happel J, Brenner H. 2012. *Low Reynolds Number Hydrodynamics: With Special Applications to Particulate Media*. Dordrecht, Neth.: Springer Neth.

Hilou E, Du D, Kuei S, Biswal SL. 2018. Interfacial energetics of two-dimensional colloidal clusters generated with a tunable anharmonic interaction potential. *Phys. Rev. Mater.* 2(2):025602

Hórvölgyi Z, Mate M, Zrinyi M. 1994. On the universal growth of two-dimensional aggregates of hydrophobed glass beads formed at the (aqueous solution of electrolyte)–air interfaces. *Colloids Surf. A* 84(2):207–16

Hórvölgyi Z, Medveczky G, Zrinyi M. 1991. Experimental study of the aggregate structures formed in the boundary layer of water-air phases. *Colloids Surf.* 60:79–95

Huang P, Guasto J, Bruer K. 2006. Direct measurement of slip velocities using three dimensional total internal reflection velocimetry. *J. Fluid Mech.* 566:447–64

Hughes B, Pailthorpe B, White L. 1981. The translational and rotational drag on a cylinder moving in a membrane. *J. Fluid Mech.* 110:349–72

Isa L, Lucas F, Wepf R, Reimhult E. 2011. Measring single nanoparticle wetting properties by freeze-fracture shadow casting cryo-scanning electro microscopy. *Nat. Commun.* 2:438

Jeffrey DJ, Onishi Y. 1984. Calculation of the resistance and mobility functions for two unequal rigid spheres in low-Reynolds-number flow. *J. Fluid Mech.* 139:261–90

Kaz DM, McGorty R, Mani M, Brenner MP, Manoharan VN. 2012. Physical ageing of the contact line on colloidal particles at liquid interfaces. *Nat. Mater.* 11(2):138–42

Kollmann M, Hund R, Rinn B, Nägele G, Zahn K, et al. 2002. Structure and tracer-diffusion in quasi–two-dimensional and strongly asymmetric magnetic colloidal mixtures. *EPL* 58(6):919–25

Koplik J, Maldarelli C. 2017. Diffusivity and hydrodynamic drag of nanoparticles at a vapor-liquid interface. *Phys. Rev. Fluids* 2(2):024303

Koplik J, Maldarelli C. 2019. Molecular dynamics of the translation and rotation of amphiphilic Janus nanoparticles at a vapor-liquid surface. *Phys. Rev. Fluids* 4(4):044201

Kralchevsky PA, Denkov ND. 2001. Capillary forces and structuring in layers of colloid particles. *Curr. Opin. Colloid Interface Sci.* 6(4):383–401

Kralchevsky PA, Denkov ND, Danov KD. 2001. Particles with an undulated contact line at a fluid interface: interaction between capillary quadrupoles and rheology of particulate monolayers. *Langmuir* 17(24):7694–705

Kralchevsky PA, Nagayama K. 1994. Capillary forces between colloidal particles. *Langmuir* 10(1):23–36

Kralchevsky PA, Nagayama K. 2000. Capillary interactions between particles bound to interfaces, liquid films and biomembranes. *Adv. Colloid Interface Sci.* 85:145–92

Kralchevsky PA, Nagayama K. 2001. *Particles at Fluid Interfaces and Membranes: Attachment of Colloid Particles and Proteins to Interfaces and Formation of Two Dimensional Arrays*. Amsterdam: Elsevier

Lauga E, Brenner M, Stone H. 2007. Microfluidics: the no-slip boundary condition. In *Springer Handbook of Experimental Fluid Dynamics*, ed. C Tropea, AL Yarin, JF Foss, pp. 1219–40. Berlin: Springer

Lee T, Charrault E, Neto C. 2014. Interfacial slip on rough, patterned and soft surfaces: a review of experiments and simulations. *Adv. Colloid Interface Sci.* 210:21–38

Löwen H, Messina R, Hoffmann N, Likos CN, Eisenmann C, et al. 2005. Colloidal layers in magnetic fields and under shear flow. *J. Phys. Condens. Matter* 17(45):S3379

Lumay G, Obara N, Weyer F, Vandewalle N. 2013. Self-assembled magnetocapillary swimmers. *Soft Matter* 9(8):2420–25

Luo H, Pozrikidis C. 2008. Effect of surface slip on stokes flow past a spherical particle in infinite fluid and near a plane wall. *J. Eng. Math.* 62:1–21

Maestro A, Bonales LJ, Ritacco H, Fischer TM, Rubio RG, Ortega F. 2011. Surface rheology: macro-and microrheology of poly(*tert*-butyl acrylate) monolayers. *Soft Matter* 7(17):7761–71

Maestro A, Guzmán E, Ortega F, Rubio RG. 2014. Contact angle of micro-and nanoparticles at fluid interfaces. *Curr. Opin. Colloid Interface Sci.* 19(4):355–67

Maestro A, Santini E, Guzmán E. 2018. Physico-chemical foundations of particle-laden fluid interfaces. *Eur. Phys. J. E* 41(8):97

Masoud H, Stone HA. 2019. The reciprocal theorem in fluid dynamics and transport phenomena. *J. Fluid Mech.* 879:P1

McBride S, Law B. 2009. Viscosity dependent liquid slip at molecularly smooth hydrophobic surfaces. *Phys. Rev. E* 80:060601

Mendoza AJ, Guzmán E, Martínez-Pedrero F, Ritacco H, Rubio RG, et al. 2014. Particle laden fluid interfaces: dynamics and interfacial rheology. *Adv. Colloid Interface Sci.* 206:303–19

Millett PC, Wang YU. 2011. Diffuse-interface field approach to modeling arbitrarily-shaped particles at fluid–fluid interfaces. *J. Colloid Interface Sci.* 353(1):46–51

Neto C, Evans DR, Bonaccurso E, Butt HJ, Craig VSJ. 2005. Boundary slip in newtonian liquids: a review of experimental studies. *Rep. Progress Phys.* 68(12):2859–97

Nicolson MM. 1949. The interaction between floating particles. *Math. Proc. Camb. Philos. Soc.* 45(2):288–95

Nishikawa H, Fujita M, Maenosono S, Yamaguchi Y, Okudo T. 2006. Effects of frictional force on the formation of colloidal particle monolayer during drying—study using discrete element method—[translated]. *KONA Powder Part. J.* 24:192–202

Nishikawa H, Maenosono S, Yamaguchi Y, Okubo T. 2003. Self-assembling process of colloidal particles into two-dimensional arrays induced by capillary immersion force: a simulation study with discrete element method. *J. Nanopart. Res.* 5(1–2):103–10

Oettel M, Dietrich S. 2008. Colloidal interactions at fluid interfaces. *Langmuir* 24:1425–41

Oettel M, Dominguez A, Dietrich S. 2005. Effective capillary interaction of spherical particles at fluid interfaces. *Phys. Rev. E* 71:051401

O'Neill M, Ranger K, Brenner H. 1985. Slip at the surface of a translating-rotating sphere bisected by a free surface bounding a semi infinite viscous fluid: removal of the contact line singularity. *Phys. Fluids* 29:913–24

Onoda GY. 1985. Direct observation of two-dimensional, dynamic clustering and ordering with colloids. *Phys. Rev. Lett.* 55(2):226–29

Paunov VN. 2003. Novel method for determining the three phase contact angle of colloid particle adsorbed at an air–water or oil–water interface. *Langmuir* 19:7970–76

Peng Y, Chen W, Fischer T, Weitz D, Tong P. 2008. Short-time self-diffusion of nearly hard spheres at an oil–water interface. *J. Fluid Mech.* 618:243–61

Petkov JT, Denkov ND, Danov KD, Velev OD, Aust R, Durst F. 1995. Measurement of the drag coefficient of spherical particles attached to fluid interfaces. *J. Colloid Interface Sci.* 172(1):147–54

Pieranski P. 1980. Two-dimensional interfacial colloidal crystals. *Phys. Rev. Lett.* 45(7):569–72

Pourali M, Kröger M, Vermant J, Anderson PD, Jaensson NO. 2021. Drag on a spherical particle at the air–liquid interface: interplay between compressibility, Marangoni flow, and surface viscosities. *Phys. Fluids* 33(6):062103

Pozrikidis C. 2007. Particle motion near and inside an interface. *J. Fluid Mech.* 575:333–57

Prevo B, Kuncicky D, Velev O. 2007. Engineered deposition of coatings from nano- and micro-particles: a brief review of convective assembly at high volume fraction. *Colloids Surf. A* 311:2–10

Radoev B, Nedjalkov M, Djakovich V. 1992. Brownian motion at liquid-gas interfaces. 1. Diffusion coefficeints of macroparticles at pure interfaces. *Langmuir* 8:2962–65

Rahman SE, Laal-Dehghani N, Barman S, Christopher GF. 2019a. Modifying interfacial interparticle forces to alter microstructure and viscoelasticity of densely packed particle laden interfaces. *J. Colloid Interface Sci.* 536:30–41

Rahman SE, Laal-Dehghani N, Christopher GF. 2019b. Interfacial viscoelasticity of self-assembled hydrophobic/hydrophilic particles at an air/water interface. *Langmuir* 35(40):13116–25

Rahmani AM, Wang A, Manoharan VN, Colosqui CE. 2016. Colloidal particle adsorption at liquid interfaces: capillary driven dynamics and thermally activated kinetics. *Soft Matter* 12(30):6365–72

Ranger K. 1978. The circular disk straddling the interface of a two-phase flow. *Int. J. Multiphase Flow* 4(3):263–77

Razavi S, Koplik J, Kretzschmar I. 2013. The effect of capillary bridging on the Janus particle stability at the interface of two immiscible liquids. *Soft Matter* 9(18):4585–89

Rinn B, Zahn K, Maass P, Maret G. 1999. Influence of hydrodynamic interactions on the dynamics of long-range interacting colloidal particles. *EPL* 46(4):537

Ruiz-Garcia J, Gamez-Corrales R, Ivlev BI. 1997. Foam and cluster structure formation by latex particles at the air/water interface. *Physica A* 236:97–104

Ruiz-Garcia J, Gamez-Corrales R, Ivlev BI. 1998. Formation of two-dimensional colloidal voids, soap froths, and clusters. *Phys. Rev. E* 58(1):660–63

Saffman P. 1976. Brownian motion in thin sheets of viscous fluid. *J. Fluid Mech.* 73(4):593–602

Saffman P, Delbrück M. 1975. Brownian motion in biological membranes. *PNAS* 72(8):3111–13

Samaniuk JR, Vermant J. 2014. Micro and macrorheology at fluid–fluid interfaces. *Soft Matter* 10(36):7023–33

Sendner C, Horinek D, Bocquet L, Netz RR. 2009. Interfacial water at hydrophobic and hydrophilic surfaces: slip, viscosity, and diffusion. *Langmuir* 25(18):10768–81

Sickert M, Rondelez F. 2003. Shear viscosity of Langmuir monolayers in the low-density limit. *Phys. Rev. Lett.* 90:126104

Sickert M, Rondelez F, Stone H. 2007. Single-particle brownian dynamics for characterizing the rheology of fluid Langmuir monolayers. *EPL* 79(6):66005

Snoeyink C, Barman S, Christopher GF. 2015. Contact angle distribution of particles at fluid interfaces. *Langmuir* 31(3):891–97

Stamou D, Duschl C, Johannsmann D. 2000. Long-range attraction between colloidal spheres at the air-water interface: the consequence of an irregular meniscus. *Phys. Rev. E* 62(4):5263–72

Stone HA, Ajdari A. 1998. Hydrodynamics of particles embedded in a flat surfactant layer overlying a subphase of finite depth. *J. Fluid Mech.* 369:151–73

Stone HA, Masoud H. 2015. Mobility of membrane-trapped particles. *J. Fluid Mech.* 781:494–505

Uzi A, Ostrovski Y, Levy A. 2016. Modeling and simulation of particles in gas–liquid interface. *Adv. Powder Technol.* 27(1):112–23

Vandadi V, Kang SJ, Masoud H. 2017. Reverse Marangoni surfing. *J. Fluid Mech.* 811:612–21

Vandewalle N, Clermont L, Terwagne D, Dorbolo S, Mersch E, Lumay G. 2012. Symmetry breaking in a few-body system with magnetocapillary interactions. *Phys. Rev. E* 85(4):041402

Vandewalle N, Obara N, Lumay G. 2013. Mesoscale structures from magnetocapillary self-assembly. *Eur. Phys. J. E* 36(10):127

Vassileva ND, van den Ende D, Mugele F, Mellema J. 2005. Capillary forces between spherical particles floating at a liquid–liquid interface. *Langmuir* 21(24):11190–200

Vidal A, Botto L. 2017. Slip flow past a gas–liquid interface with embedded solid particles. *J. Fluid Mech.* 813:152–74

Villa S, Boniello G, Stocco A, Nobili M. 2020. Motion of micro- and nano-particles interacting with a fluid interface. *Adv. Colloid Interface Sci.* 284:102262

Vinogradova OI, Yakubov GE. 2003. Dynamic effects on force measurements. 2. Lubrication and the atomic force microscope. *Langmuir* 19(4):1227–34

Voronov RS, Papavassiliou DV, Lee LL. 2007. Slip length and contact angle over hydrophobic surfaces. *Chem. Phys. Lett.* 441:273–76

Wurger A, Foret L. 2005. Capillary attraction of colloid particles at an aqueous interface. *J. Phys. Chem. B* 109:16435–38

Zabarankin M. 2007. Asymmetric three-dimensional Stokes flows about two fused equal spheres. *Proc. R. Soc. A* 463(2085):2329–50

Zahn K, Maret G. 1999. Two-dimensional colloidal structures responsive to external fields. *Curr. Opin. Colloid Interface Sci.* 4(1):60–65

Zahn K, Méndez-Alcaraz JM, Maret G. 1997. Hydrodynamic interactions may enhance the self-diffusion of colloidal particles. *Phys. Rev. Lett.* 79(1):175

Zhu L, Neto C, Attard P. 2012. Reliable measurements of interfacial slip by colloid probe atomic force microscopy. III. Shear-rate-dependent slip. *Langmuir* 28(7):3465–73